Chapter 7

Biomolecule-Conjugated Quantum Dot Nanosensors as Probes for Cellular Dynamic Events in Living Cells

Jung Y. Huang

Additional information is available at the end of the chapter

http://dx.doi.org/10.5772/intechopen.72858

Abstract

A single-molecule tracking/imaging technique with semiconductor quantum dot (QD) nanosensors conjugated with appropriate peptides or antibodies is appealing for probing cellular dynamic events in living cells. We developed a 2D analysis of single-molecule trajectories using normalized variance versus mean square displacement (MSD) to provide high-quality statistics sampled by nanosensors while preserving single-molecule sensitivity. This plot can be more informative than MSD alone to reflect the diffusive dynamics of a protein in its cellular environment. We illustrate the performance of this technique with selected examples, which are designed to expose the functionalities and importance in live cells. Our findings suggest that biomolecule-conjugated QD nanosensors can be used to reveal interactions, stoichiometries, and conformations of proteins, and provide an understanding of the mode of the interaction, stable states, and dynamical pathways of biomolecules in live cells.

Keywords: quantum dot, single-particle tracking, fluorescence imaging, stochastic thermodynamics, single-molecule trajectory, living cell, plasma membrane, epidermal growth factor receptor, lipid domain, actin filaments, cell-penetrating peptides

1. Introduction

Studying the movement of individual biomolecules in live cells and their interactions with the surrounding microenvironment would greatly improve our understanding of how biomolecules behave in their native cellular environment [1, 2]. Deciphering those functions and relevant regulation mechanisms is also important for developing new therapeutic strategies for diseases [2]. The major factors affecting protein mobility include local viscosity, protein–protein interaction, molecular crowding, and dimensionality of accessible space [3]. However, such factors are difficult to reconstitute in vitro using purified constituents. Therefore, there is a compelling demand for a tool to directly access the properties of the molecular assemblies

and kinetics of interaction in live cells. Single-molecule imaging and tracking based on fluorescence microscopy have been developed to meet this challenge [4, 5].

The primary factor controlling the motion of a protein in a living cell is often not the friction in the cellular medium but the interactions with its molecular partners, which often result in a transient stall or transport of molecules [3]. The binding energies between the protein of interest and its interacting partners are also of interest because regulatory processes can be mediated by changes in these binding energies. Biological media are spatially inhomogeneous, which is poorly conveyed by measuring just a few, sparse single-molecule trajectories. Thus, to fully realize the potential of a single-molecule imaging and tracking technique, an efficient and reliable analytical method is required to help extract useful information from the large amounts of trajectory data. This type of analysis usually involves the computing of the mean square displacement (MSD) along the trajectories of the molecules [6, 7].

The key component of the single-molecule imaging and tracking technique is a set of bright fluorophores with different emission wavelengths. Semiconductor quantum dots (QDs) have unique optical properties, such as high emission efficiency, wavelength tunability, and long-term stability, which make them appealing as *in vivo* and *in vitro* fluorophores [8, 9]. The ability to make water-soluble QDs that can be targeted to specific biomolecules has led to a variety of applications in cellular sensing and imaging. For example, Zhang et al. developed a QDs-labeled silica nanoprobe for the detection of apoptotic cells in response to therapy [10]. Different classes of fluorescent nanoprobes were also developed for the imaging of cellular metal ions [11], which serve as essential cofactors in energy metabolism, signal transduction, and nucleic acid processing. Recently, Jainb et al. developed a synthetic technique of QD immunoconstructs by coupling antibodies (Ab) to QD [12]. The resulting QD-Ab conjugates can maintain a high and stable quantum yield for *in vivo* environments and acts as an ideal nanosensor to specific antigene. Therefore, a molecular-level of understanding of the cellular functions in the context of their native environments becomes possible.

Labeled biomolecules in their native environments can be considered a mesosystem with a length scale ranging from a few nanometers to <1 μm. Our understanding of thermodynamically equilibrated mesosystems roots solidly in equilibrium statistical mechanics. For small deviations from the equilibrium, researchers can invoke the linear response theory to relate the transport properties caused by the external fields to the equilibrium correlation functions. Beyond this linear response regime, no universally exact results are currently available [13].

Under non-equilibrium conditions, the temperature of a mesosystem in solution remains well-defined, yielding a value that is the same as that of the embedding solution [13]. For a complex biomolecular system comprised of N relatively rigid domains, the configuration can be described by a 3N–dimensional vector of Cartesian coordinates. The interactions among these rigid units introduce cooperative couplings between the units that yield a separation of time scales [14]. The resulting time-scale separation occurs between the observable slow degrees of freedom of the system and the fast ones that are made up by both the system and thermal bath. The collection of the slow degrees of freedom offers a natural approach to define the states of a system. The state changes with time, either due to the external driving or from ever-present thermal fluctuations that trace out a trajectory. The thermodynamic quantities defined along the trajectories follow a distribution with some universal constraints [14].

Stochastic thermodynamics is a relatively new subject, which focuses on the description of the individual trajectories [14]. This framework can serve as a solid foundation for single-molecule technique but has not been sufficiently clarified in the literature. In this chapter, we first briefly review some basic concepts of stochastic thermodynamics that are specifically relevant to the analysis of the trajectories from a single-molecule optical imaging and tracking technique. Repetitive measurements of the cellular locations $\tilde{x}(t)$ of nanosensors provide an entire history of that observation. Provided that the repetitive measurements could scan all of the system degrees of freedom, the time evolution of the system may be encoded into the trace of this nanosensor. Based on this understanding, we illustrated the procedures of implementing such concepts in the analysis of trajectories for receptor proteins on the plasma membranes of living cells and obtained useful information from this important system.

Note that the separation of time scales can also render the dimensionality of a mesosystem much lower than the 3N–dimensional coordinate space. Thus, the trajectories through 3N–dimensional space are effectively restrained to an intrinsic manifold of much lower dimensionality [15, 16]. To show the usefulness of this concept in single molecule tracking, we took advantage of the brightness and photostability of QDs to investigate the translocation behavior of the human immunodeficiency virus 1 (HIV-1) transactivator of transcription peptide (TatP)-conjugated quantum dot (TatP-QD) nanosensors in complex cellular terrains [17]. As TatP-QDs translocate across the plasma membranes of living cells, the particles can be viewed as nanoscale pens [18] to record the influence of the hierarchical structure of the cellular environment on TatP-QD trajectories. Analysis of the resulting three-dimensional (3D) trajectories disclosed the interaction between the TatP-QDs and bioactive groups on the plasma membrane [19, 20]. An understanding of the cellular uptake of TatP is also essential for the development of TatP-based delivery strategies for therapeutic applications.

This chapter aims to expose the connections between the framework of stochastic thermodynamics, single-molecule optical tracking, and trajectory analysis. Applications were mentioned to illustrate the type of information that can be deduced from these studies. The chapter is not a complete review on relevant subjects. Many important research studies have not been mentioned or referred. The author simply hopes this article will encourage interested readers to design new experiments that would fill in the holes of this article.

2. Formalism of single-molecule trajectory analysis

2.1. A brief overview of stochastic thermodynamics

For a mesosystem in contact with a heat bath, the probability of finding it in a specific microstate is given by the Boltzmann factor (i.e., $\exp[-U(x,p)/k_BT\ ]$ [13], where U denotes the total internal energy with x and p being the generalized coordinates and momentums of particles enclosed in the system). Stochastic thermodynamics provides the framework for extending the notions of work, heat and entropy production from classical thermodynamics to individual trajectories of non-equilibrium processes. It brings out the fluctuation-dissipation theorems (FDT) to constrain the probability distributions for work, heat, and entropy production along each trajectory [14]. Some milestone developments in this discipline include:

1) Both the steady-state and transient FDT were valid for a large class of systems, including chaotic dynamics [21], driven Langevin dynamics [22], and driven diffusive dynamics [23].

2) The Jarzynski relation (JR) was derived [24, 25], which relates the free energy difference between two equilibrium states to the average work done to drive the system from one state to the other along a non-equilibrium process. For non-equilibrium systems driven by time-dependent forces, a refinement of the JR became extremely useful to determine the free energy landscapes of biomolecules [26, 27].

3) The exchanged heat and applied work could also be rigorously defined along individual trajectories of the driven Brownian motion. The entropy produced in a medium could thereby be related to the stochastic action, which also serves as the weight of trajectories [28].

2.2. Trajectory analysis of single-molecule stochastic processes

2.2.1. Two-dimensional plot of normalized variance and mean square displacement of single-molecule trajectories

In a living cell, a biomolecule subjected to random influences can explore its possible outcomes and evolve to yield dispersion over state space. This evolution contains contributions from both deterministic and stochastic forces. The time-scale separation mentioned above implies that the dynamics will become Markovian and follow a generalized Langevin equation [29]

$$\partial_t \vec{x}_k(t) = -\nabla_k U\left(\vec{x}_k(t)\right)/\gamma \quad + \sqrt{2D}dW_t = F_k(t)/\gamma \quad + f_k(t)/\gamma, \tag{1}$$

where subindex k represents the k-th particle at the position $\vec{x_k}$. The frictional parameter γ is relevant to the diffusion coefficient D with $\gamma.D = k_B T$. The total deterministic force acting on the diffusive particle is expressed as $F_k(t)$. The stochastic force $f_k(t)$ follows the Weiner process with zero mean and a delta correlation of $< f_k(t+\tau) \cdot f_k(t) >= 2\gamma k_B T \delta(\tau)$.

By rewriting Eq. (1) as $dx_k = F_k/\gamma \quad \cdot dt + \sqrt{2D}dW_t$ and invoking the stochastic chain rule, we derived an equation for the square displacement [30]

$$(dx_k)^2 = 2F_k/\gamma \cdot x_k dt + 2Ddt + 2\sqrt{2D}x_k dW_t. \tag{2}$$

From Eq. (2), we further derived the local MSD $\overline{{R_k}^2}$ as

$$\overline{{R_k}^2} = \overline{{dx_k}^2} = 2/\gamma \quad \cdot \overline{F_k x_k}\, dt + 2Ddt, \tag{3}$$

and similarly, the variance of the square displacement $Var\left({dx_k}^2\right) = \overline{\left({dx_k}^2\right)^2} - \left[\,\overline{{dx_k}^2}\,\right]^2$ as

$$Var\left({dx_k}^2\right) = 8D\,(\overline{x_k})^2 dt - (4/\gamma) \cdot Var[F_k x_k]\,(dt)^2, \tag{4}$$

where *Var*[.] denotes the variance operation. A normalized variance of square displacement was defined as $V\left({R_k}^2\right) = Var\left[{R_k}^2\right]/\left(\overline{{R_k}^2}\right)^2$, which yielded [30]

$$V(R_k^2) = \frac{(2\gamma/dt\ )(\overline{x_k})^2 - Var[F_k x_k]}{\gamma D + \overline{F_k x_k}}. \tag{5}$$

We applied this function to display the relative influence on the trajectories by deterministic forces $F_k(t)$ and by the stochastic force f_k. As particles diffuse under a force field, $V(R^2)$ increases with force strength [30]. As a particle diffuses near a short-range force field, it can be stalled briefly by the force field, resulting in large variances in the diffusion step size. In contrast, $V\left(\overline{R_\tau^2}\right)$ will fall below the free diffusion limit ($V(R^2) = 2$) when a probing particle moves in an environment where its surrounding medium can be polarized by the particle either electrically or orientationally [30]. This dressing effect could lead to smaller variances, and therefore smaller $V(R^2)$. We proposed a histogram of $\overline{R_\tau^2}$ and normalized variance $V(R^2)$ in a contour plot. Here, the MSD values were used to quantify the diffusion of a probing particle, and $V\left(\overline{R_\tau^2}\right)$ revealed the nature (e.g., deterministic or stochastic) of the interactive forces involved [31].

In the following, we presented some simulated results to illustrate the features of this ad hoc data-driven methodology in the framework of stochastic thermodynamics. Using Eq. (1), we first simulated 2D motions of Brownian particles in a force field, which had a potential energy surface $U\left(\vec{x}\right) = k\left(\vec{x} - \vec{x}_0\right)^T \cdot \left(\vec{x} - \vec{x}_0\right)/2 \ + \sum_i \alpha_i \exp\left[-\left(\vec{x} - \vec{x}_{i0}\right)^T \cdot \left(\vec{x} - \vec{x}_{i0}\right)/w_i^2\right]$ (see **Figure 1a**). The potential energy surface comprised two isotropic Gaussian wells and a long-range harmonic potential to prevent the particle from drifting off to infinity. The central positions of the harmonic potential and two Gaussian wells are located at (3, 3), (2, 0) and (0, 2), respectively. The strength parameters of the harmonic and Gaussian potentials were chosen to yield deterministic forces, which were a factor of 0.14 and 3.8 to that of the stochastic force

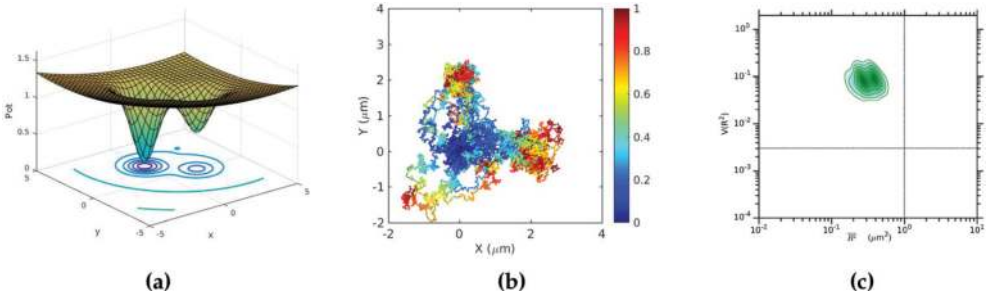

Figure 1 (a) Plot of the potential energy surface with $U\left(\vec{x}\right) = 0.05\left[0.1\left(\vec{x} - \vec{x}_0\right)^T \cdot \left(\vec{x} - \vec{x}_0\right) - 11\left(e^{-\left(\vec{x}-\vec{x}_{10}\right)^T \cdot \left(\vec{x}-\vec{x}_{10}\right)} + 2e^{-\left(\vec{x}-\vec{x}_{20}\right)^T \cdot \left(\vec{x}-\vec{x}_{20}\right)}\right)\right]$, where $\vec{x}_0 = (3,3)$, $\vec{x}_{10} = (2,0)$, and $\vec{x}_{20} = (0,2)$. The energy surface was shifted upwardly by 1 to make the contour plot visible. (b) Twenty-five randomly selected trajectories were displayed with appearing times coded by different colors. (c) the statistics of 500 trajectories were summarized in the $V(R^2)$-$\overline{R_\tau^2}$ plot, exhibiting a peak at $V(R^2) \simeq 0.1$, $\overline{R_\tau^2} \simeq 0.27$ and 0.4.

($\sqrt{2D}/\gamma = 0.35$). We updated the locations of the Brownian particles every 0.01 s using the Euler–Maruyama solver, starting at initial position (0, 0). We generated a total of 500 trajectories, each of a 10 s duration. **Figure 1b** displays 25 randomly selected trajectories with appearing times coded by different colors.

As the particles move toward the center of the harmonic potential, they are attracted to the two Gaussian wells. Well 2, centered at (2, 0), had the same width but was deeper than well 1 by a factor of 2. Thus, at the end of the simulation, the particles near (2, 0) were about twice that of those near well 1. As displayed in **Figure 1c**, the diffusion yielded a dual-peak structure at $V(R^2) \simeq 0.1$, $\overline{R_\tau{}^2} \simeq 0.27$ and 0.4 in the $V(R^2)$-$\overline{R_\tau{}^2}$ plot, indicating that as a particle repeatedly visits or stays in a spatial region, the characteristic $V\left(\overline{R_\tau{}^2}\right)$ and $\overline{R_\tau{}^2}$ of the location will be imposed on the trajectories.

Next, we reduced the width of well 2 by a factor 3 while keeping its depth at the same value (see **Figure 2a**. At the end of the simulation, the particles located near (0, 2) became one third that of those near Well 1 (see red spots in **Figure 2b**). **Figure 2c** displays a peak at $V(R^2) \simeq 0.25$ and $\overline{R_\tau{}^2} \simeq 0.25$. Although the population at well 2 was lower, its influence on the trajectories with a higher $V(R^2)$ value was visible. For a brief summary of this simulation, we would like to point out an attractive feature of the $V(R^2)$-$\overline{R_\tau{}^2}$ plot. When a molecule repeatedly visits or stays in a spatial region, the characteristic $V\left(\overline{R_\tau{}^2}\right)$ and $\overline{R_\tau{}^2}$ of the location will be imposed on the trajectories, which then results in the formation of a peak at the corresponding position on the plot.

We used the hidden Markov model (HMM) to further reveal the dynamics by identifying the underlying state changes and their corresponding occupation probability π_i and transition rates $r_{i\to j}$. Note that in the ergodic limit, the system will reach an equilibrium with a distribution of

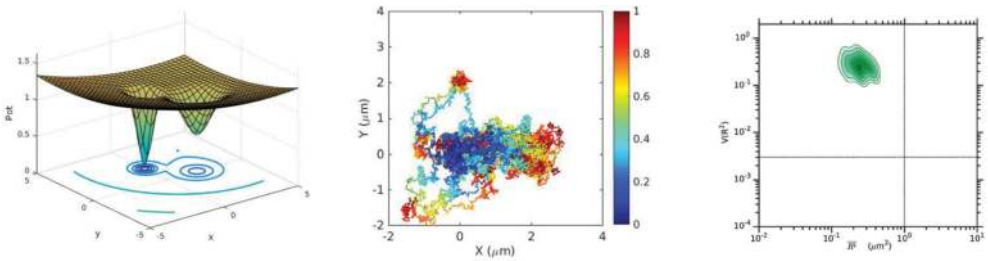

Figure 2 (a) Plot of the potential energy surface with $U\left(\vec{x}\right) = 0.05\left[0.1\left(\vec{x}-\vec{x}_0\right)^T \cdot \left(\vec{x}-\vec{x}_0\right) - 11\left(e^{-\left(\vec{x}-\vec{x}_{10}\right)^T \cdot \left(\vec{x}-\vec{x}_{10}\right)} + 2e^{-3\left(\vec{x}-\vec{x}_{20}\right)^T \cdot \left(\vec{x}-\vec{x}_{20}\right)}\right)\right]$, where $\vec{x}_0 = (3,3)$, $\vec{x}_{10} = (2,0)$, and $\vec{x}_{20} = (0,2)$. The energy surface was shifted upwardly by 1 to make the contour plot visible. (b) twenty-five randomly selected trajectories from the simulation were displayed. (c) the statistics of 500 trajectories were summarized in the $V(R^2)$-$\overline{R_\tau{}^2}$ plot, exhibiting a peak at $V(R^2) \simeq 0.25$, $\overline{R_\tau{}^2} \simeq 0.25$.

$p_{eq}(x) = e^{-\beta U(x)}/Z_{eq}$, where $U(x)$ is the potential of mean force (PMF) with x denoting the generalized coordinates, and Z_{eq} representing the equilibrium partition function [32]. We can measure the static dispersion of the system using entropy $S\left[p_{eq}(x)\right] = -\int dx p_{eq}(x) \ln\left[p_{eq}(x)\right]$ as a caliber [14, 33]. For non-equilibrium processes, the entropy produced along a trajectory with time resolution Δt becomes $S(\Delta t) \equiv \sum_{i,j}^{N} \pi_i r_{i\to j}(\Delta t) \ln r_{i\to j}(\Delta t)$, which required averaging over the stochastic trajectories to display the degree of dynamic dispersion. For coarser time resolutions (i.e., larger Δt), the transition rates converged to their equilibrium values and the information about the dynamics is lost.

2.2.2. *Spectral-embedding analysis of single-molecule trajectories*

Conformational trajectories of a biomolecular system, comprising N relatively rigid domains, can be displayed in a 3N–dimensional phase space. As noted above, cooperative couplings between these rigid units often yield a separation of time scales, which causes the system's slow degrees of freedom to be separated from the fast ones made up by the system and thermal bath. An intrinsic manifold of much lower dimensionality is thus embedded in the high-dimensional configuration trajectories. Unfortunately, the projection of dynamical configurations $f: \ R^{3N} \to M(R^m)$ into a reduced dimensional space, which is specified by m collective variables $\tilde{\phi} = [\phi_1, \phi_2, \ldots, \phi_m] \in M$, is highly nonlinear and unavailable from analytical theory. The first issue encountered in depicting the complex dynamics in a low-dimensional space is how to identify a set of appropriate slow variables $\tilde{\phi}$. In recent years, a number of machine learning approaches have been developed to infer such mappings by discovering low-dimensional manifolds within high-dimensional trajectories [15].

Recently, Wang and Ferguson successfully applied the generalized Takens Delay Embedding Theorem [34] to retrieve a low-dimensional representation of the free energy landscape from univariate time series of single-molecule physical observable. The authors also determined that the univariate time series could be expanded into a high-dimensional space in which the dynamics were equivalent to those of the molecular motions in real space. Single-molecule optical techniques based on a variety of nanosensors can provide the time series of experimentally accessible observables. By measuring the impact of cellular environments on the trajectory ensemble of those nanosensors, it is possible to reveal the influence of the cellular environments. **Figure 3** presents a conceptual drawing to illustrate the translocation process of biomolecule-conjugated quantum dot nanosensors across the cellular plasma membrane.

We assumed the trajectory ensemble $\vec{x}\ (t)$ of the nanosensors to be generated by a stochastic process governed by Eq. (1). Here, $\vec{x}\ (t)$ was implicitly dependent on the generalized coordinates of the fast degrees of freedom $\vec{\xi}_i(t)$ because the probing particles could move in n different realizations of the local environment with interaction potentials $U_i\left(\vec{x}\ \left(\vec{\xi}\right)\right); i = 1, .., n$. In the following, we will describe a projection of $\vec{x}\ (t)$ on slow degrees of freedom to disclose the influences of $U_i\left(\vec{x}\ \left(\vec{\xi}\right)\right); i = 1, .., n$.

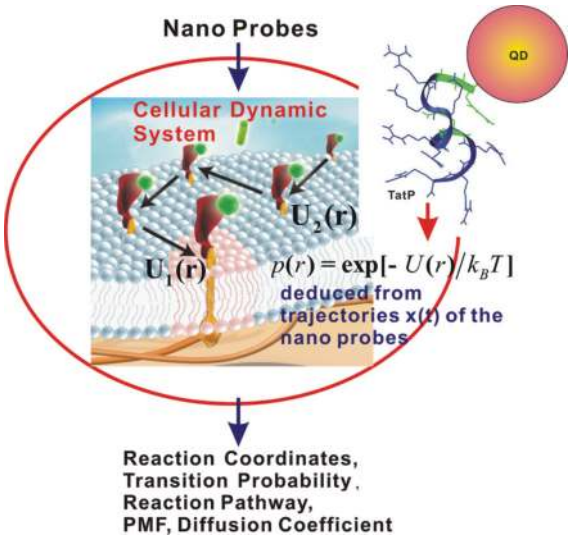

Figure 3 A schematic showing the translocation process of biomolecule-conjugated QDs that depict cellular dynamic processes by recording the impact of cellular environments on the trajectory ensemble of the nanosensors.

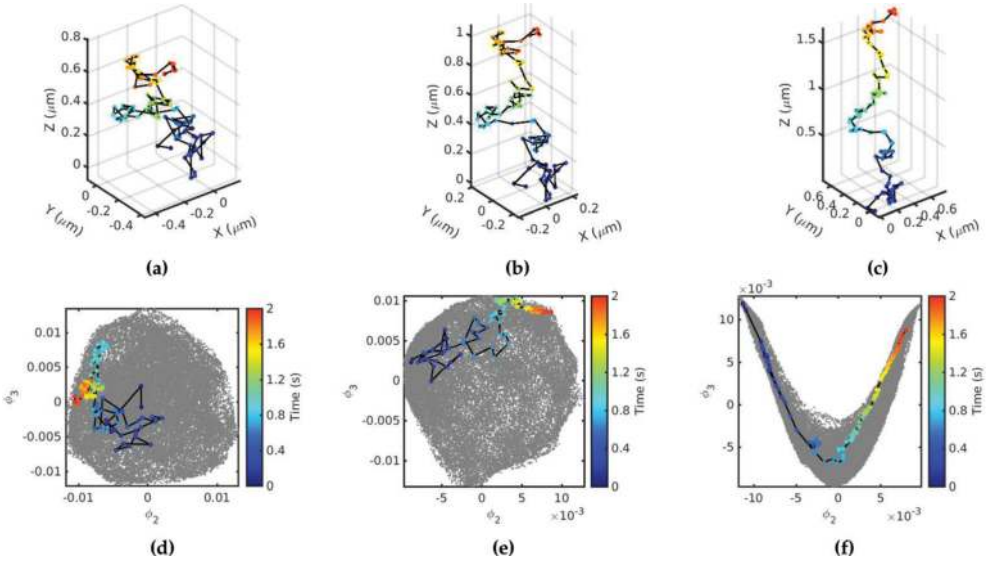

Figure 4 Simulated trajectories of particle diffusing (a,d) isotropically with $|F_k/f_k| = 0$ $D = 0.05\,\mu m^2/s$) or under a unidirectional force field with (b,e) $|F_k/f_k| = 0.01$ and (c,f) $|F_k/f_k| = 0.03$ were displayed with appearing times color-coded. For each case, a total of 300 simulated trajectories (gray in d, e, and f) were shown on a low-dimensional manifold of two principal spectral-embedding eigenvectors. The trajectories shown in (a, b, and c) were reproduced on the manifold with appearing times color-coded.

We first simulated 3D Brownian motion with Eq. (1) under the three conditions: isotropic diffusion with $|F_k/f_k| = 0$, $D = 0.05\,\mu m^2/s$ and under z-unidirectional force fields with $|F_k/f_k| = 0.01$ and 0.03. Starting at the origin we generated an ensemble of 300 trajectories for each case. Every trajectory contained 100 diffusion steps with a time resolution of 0.02 s. We display three typical trajectories in **Figure 4a–c**, which clearly exhibit increased spread along z due to the action of the unidirectional force field.

Spectral-embedding analysis can be implemented in the diffusion-map framework to enable an efficient construction of good slow observables and thereby can expose the low-dimensional manifolds underlying the high-dimensional datasets [35]. A graph-based method provided a discretized approximation of the manifold for efficiently constructing eigen-decomposition of the datasets [36]. We assembled the time-delayed vector $\tilde{x}_k(t) = \left[\vec{x}_k^{\,(i)}\right]_{i=1,s}$ $= \left[\vec{x}_k(0), \vec{x}_k(\tau), \ldots, \vec{x}_k((s-1)\tau)\right]$ and projected the time series onto a low-dimensional manifold by exploiting the spectral-embedding technique [35]. The first eigenvector was trivial because its eigenvalue gave only the data density in a cluster. We then focused on the next two eigenvectors, ϕ_2 and ϕ_3, which offered the most critical information on the interactions between the nanosensors and their environments. **Figure 4d–f** display the ϕ_2-ϕ_3 plot of the simulated trajectory data, shown in gray. For comparison, the trajectories presented in **Figure 4a–c** are also reproduced here with appearing times color-coded. A V-shaped distribution in the ϕ_2-ϕ_3 plot developed gradually with force field strength, suggesting the V-shaped feature was a useful indicator of directed movement under a force field [17].

In **Figure 5a**, the isotropic diffusion produced statistics with a clear peak at $V(R^2) \simeq 0.0023$ and $\overline{R_\tau{}^2} \simeq 0.86$ in the $V(R^2)$-$\overline{R_\tau{}^2}$ plot. As field strength F_k/f_k increased to 0.03, the peak shifted upwardly to $V(R^2) \simeq 0.014$ and $\overline{R_\tau{}^2} \simeq 0.59$, indicating a larger diffusion stepsize variation under the force field. Thus, both of the $V(R^2)$-$\overline{R_\tau{}^2}$ analysis and spectral-embedding technique can reveal the influences of the cellular environment on nanosensors but from different viewpoints.

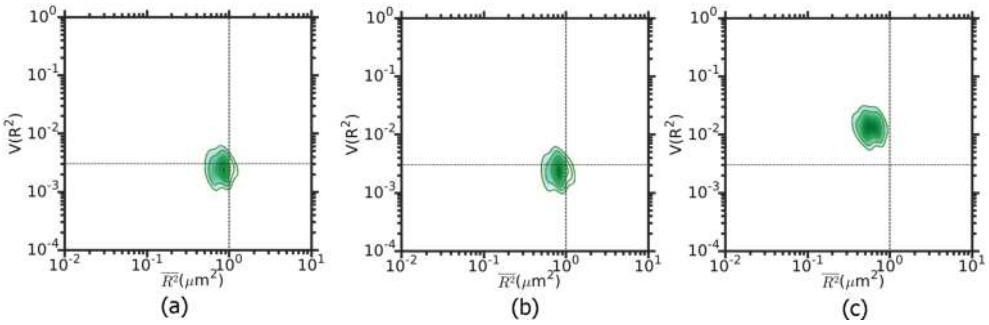

Figure 5 2D contour plot of $\left[V\left(\overline{R_\tau{}^2}\right)\right]$-$\overline{[R_\tau(t)]^2}$ histogram from simulated trajectories of particle diffusing (a) isotropically with $|F_k/f_k| = 0$, $D = 0.05\,\mu m^2/s$) or under a unidirectional force field with (b) $|F_k/f_k| = 0.01$ and (c)$|F_k/f_k| = 0.03$.

3. Apparatus and experimental procedures

3.1. Optical setup

The schematic of our single-particle fluorescence microscopy apparatus with light-sheet excitation is shown in **Figure 6a**. The output beam from a solid-state laser with different wavelengths was shaped into a light sheet of 3 μm thickness at the beam waist, yielding a diffraction-limited beam propagation with a Rayleigh range of 41 μm in the x direction. By using a galvanometer scanner, the light sheet can be positioned at a sample in a range of 34 μm along the y and z directions with an accuracy of 0.5 μm [17].

A 60 × 1.45 numerical aperture oil immersion objective lens (APON 60XOTIRFM, Olympus) was used to ensure both high spatial resolution and high photon collection efficiency. However, this objective lens had a limited depth of field (∼500 nm). For accurately resolving the depth of a fluorophore, we exploited the astigmatism created by a cylindrical lens (CL2). The combination of the CL2 (f = 100 cm and an imaging lens (f = 20 cm) with a separation of 5.5 cm generates an effective focal length of 17.5 cm on the sagittal focal plane and 20 cm on the tangential focal plane, which encodes the fluorophore depth as an elliptically shaped point spread function (PSF; see **Figure 6a**). We also inserted an electrically tunable lens (ETL) at the pupil plane of a 4f optical system (formed by the relay lens and the imaging lens) to enable fast acquisition of images at different depths. The fluorescence images of fluorophores on living cells were recorded with a scientific complementary metal-oxide semiconductor (sCMOS) camera (ORCA-Flash 4.0 V2, Hamamatsu). Fluorescence images of quantum dot nanosensors on a living HeLa cell acquired with this apparatus are displayed without CL2 in **Figure 6b** and with CL2 in **Figure 6c**, respectively. Elliptically shaped spots were observable, which were localized within 1 μm of the imaging plane at a lateral accuracy of 27 nm and an axial accuracy of 52 nm [17].

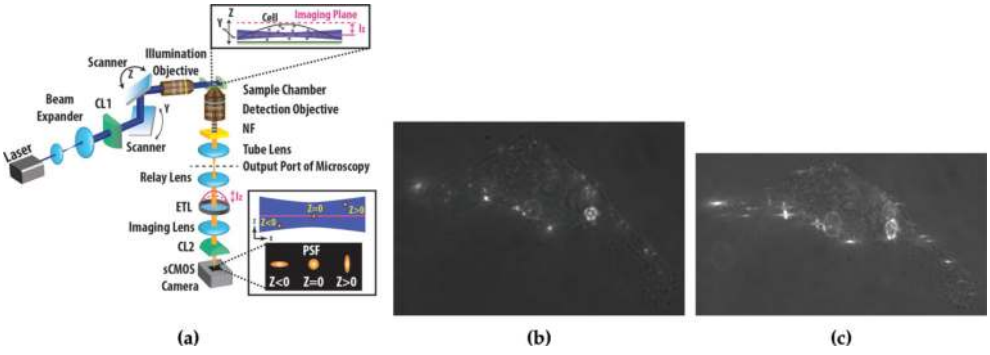

Figure 6 (a) Schematic of the light-sheet microscope used to record 3D trajectories of probing nanoparticles in a living cell. The excitation beam was shaped to form a 3 μm-thick light sheet, giving a Rayleigh range of 41 μm. A two-dimensional (2D) scanner was inserted to move the light sheet by 34 μm along the y and z directions at the sample position. The imaging arm was perpendicular to the excitation direction, and an imaging plane in the sample was relayed and imaged to a sCMOS camera. The position of the imaging plane was adjusted using an ETL to yield a set of depth-resolved images. An astigmatism was introduced using a CL2 to encode information on the fluorophore depth into an elliptically distorted point spread function. Fluorescence images of Qdot585 for a living HeLa cell acquired with this apparatus without CL2 (b) or with CL2 (c) are shown. (a) has been reproduced from ref. [17].

3.2. Linking localized coordinates of nanosensors for generating 3D trajectories

Single-particle trajectories were recorded for as long as 100 s, with a frame time of 25 ms. The localized coordinates of the nanosensors were extracted from a set of images acquired by synchronously scanning the light sheet and imaging focal plane. Connecting the acquired location coordinates to generate 3D trajectories was challenging. We first carried out multiple particle tracking by solving a linear-assignment problem [37] to identify the assignment matrix between the measured location coordinates and their predicted positions. A Kalman filter was also implemented to provide an optimal estimate of Brownian motion in the presence of Gaussian noise [38]. To verify the functionality of our linking method for 3D–trajectory generation, we simulated a group of particles diffusing in a spatial region with a different number of densities and diffusion coefficients. The resulting 3D trajectories were coarse-grained to yield time series of location coordinates with the same data-taking procedure as that used in our light-sheet microscope. The simulation results are shown in **Figure 7**, which indicated a particle density lower than 0.01 $/\mu m^2$, $D < 0.1\,\mu m^2/s$, and a linking accuracy that could be higher than 98%.

3.3. Cell culture and reagents

HeLa and A431 cells were cultured in Dulbecco's Modified Eagle's medium (DMEM) without phenol red supplemented with 10% (v/v) fetal bovine serum. MCF12A cells were cultured in a 1:1 mixture of DMEM and Ham's F12 medium containing 20 ng/mL Human EGF, 0.01 mg/mL bovine insulin, 500 ng/mL hydrocortisone, and 5%(v/v) horse serum [39]. Before single-molecule live-cell imaging was performed, the cells were plated in an eight-well chamber slide. When a 70% confluence was reached, HeLa and A431 cells were deprived of serum for 24 h and MCF12A cells for 3 h.

To label EGFR, anti-EGFR antibody (10 nM; Thermo Scientific) was conjugated with Qdot525 (from Invitrogen, Carlsbad, CA, USA). Cells were incubated with the EGFR-Ab-Qdot525 for 15 min and washed three times with phosphate buffered saline (PBS). Fluorescent EGF (EGF-Qdot585) was synthesized by conjugating biotin-EGF (from Invitrogen) to Qdot585-streptavidin in PBS. To activate EGFRs, cells were incubated in the presence of 40 ng/mL EGF-Qdot585 [31, 39].

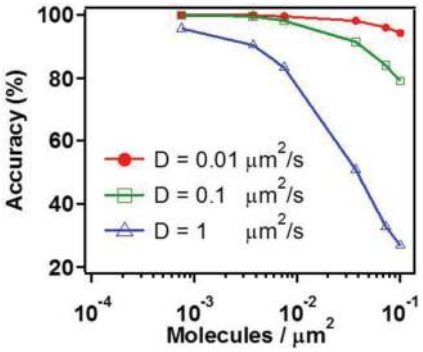

Figure 7 Linking accuracy of localized coordinates as a function of number density of Brownian particles. Trajectories of a group of particles diffusing in a spatial region with different particle densities and diffusion coefficients were simulated with Eq. (1) and then coarse-grained with the same sampling scheme as that used in our scanning light-sheet microscope.

To sequester cholesterol molecules on the plasma membranes, cells were treated with 10 μg/ml nystatin for 1 h before staining with either the antibody or EGF. To disrupt the actin filaments, the cells were pretreated with 10 μm cytochalasin D (Cyto D) for 1 h.

The N terminals of the Tat peptides (from Invitrogen) were biotinylated. Conjugated TatP-QDs were prepared by incubating 20-nm diameter streptavidin-coated Qdot585 in PBS with excess biotinylated TatP (5 μm TatP:50 nM Qdot585) at room temperature for 30 min. Although streptavidin is a tetramer and each subunit can bind biotin with equal affinity, the covalent attachment of streptavidin to the surface of a quantum dot makes two of the four binding sites inaccessible to the biotinylated TatP. As each QD has approximately 5 to 10 streptavidin molecules on its surface, we estimated that an average of 14 Tat peptides was conjugated to each QD.

4. Experimental results

The plasma membrane of a living cell is not merely a sea of lipids and proteins, but is more complex with individual components organized into spatially distinct compartments to yield strategic advantages for protein function and signaling [40]. Organizing proteins and lipids into nanodomains could also shield these assemblies from other proteins to tailor specific interactions, thereby mediating signal transduction to relay cellular messages from the external environment to the nucleus [41, 42].

The first event of cellular signaling occurs at various types of receptor proteins in the plasma membrane. To faithfully sense a signal that varies in space and time, live cells face an optimization problem of placing a set of distributed and mobile receptors by balancing two opposing objectives [43]: 1) the need to locally assemble the nanosensors to reduce the estimation noise; and 2) the need to spread these nanosensors to reduce spatial sensing errors. Receptor signaling dysregulation is attributed to the pathogenesis of several diseases [44, 45]. Therefore, understanding the interactions, molecular processes and relevant structures of such signaling assemblies is imperative. One such receptor protein is the epidermal growth factor receptor (EGFR), which can drive cell growth and survival [44]. There is tremendous interest in unraveling how those transducing proteins diffuse and interact on plasma membranes of living cells. However, it remains a challenge to study these cellular events at the single-molecule level in a live cell as living cells are highly heterogeneous and stochastically dynamic.

Based on our current knowledge of molecular diffusion in the plasma membrane, there are two types of interactions between a receptor and its local environment [46, 47]. First, the protein can induce a local ordering of the surrounding lipid molecules via a lipid-protein interaction. In addition, the cortical actin framework can induce membrane compartments [30]. To study the diffusing behaviors of EGFRs and the interaction with their cellular environment, we tagged EGFRs with antibody-conjugated quantum dots (Qdot525-Ab) and exploited fluorescent EGF, which was synthesized by conjugating EGF with quantum dots (QD585-EGF), to activate the EGFRs. By using this scheme, we could study the diffusive dynamics of paired EGFRs by selecting a pair of liganded and unliganded EGFR or a pair of liganded EGFRs, and follow their relative motions [31]. To appreciate the potential of biomolecule-

conjugated QD nanosensors in a live cell study, we will briefly review some previous results of applying single-molecule tracking techniques to EGFR studies [31, 39].

4.1. Ligand binding induced receptor protein translocation in plasma membranes of living cells

Typical single-molecule tracks of unliganded Qdot525-Ab-EGFR and liganded Qdot585-EGF-EGFR on live cells exhibited confined diffusion interspaced by directed movement [31]. We binned the measured MSD in a histogram to deduce the probability density function of the diffusion coefficient. **Figure 8a** shows the data taken at a frame rate of $\tau = 25$ ms. For unliganded EGFR at rest, two sets of diffusers were observed with the diffusion coefficient of the fast species peaking at 9 $\mu m^2/s$ and the slower one at 0.3 $\mu m^2/s$. EGF activation suppressed the population of $0.3\,\mu m^2/s < D < 6\ \mu m^2/s$, whereas it increased the populations of D $D \leq 0.1\ \mu m^2/s$ and $D = 9\ \mu m^2/s$. It is clearly shown that receptor ligation can affect the diffusion of EGFR and leads to a population change in the two diffusion states.

We used Cytochalasin D to disrupt the cellular actin frameworks. As presented in **Figure 8b**, the major population of unliganded Qdot525-Ab-EGFR (open symbols) on EGF-activated cells shifted from the slow state ($D < 0.1\ \mu m^2/s$) to the fast state ($0.1\,\mu m^2/s < D < 2\ \mu m^2/s$) after Cytochalasin D treatment. This influence is even more pronounced on liganded Qdot585-EGF-EGFR (filled symbols). As pointed out previously, the primary effector controlling the motion of a protein in a living cell is often not due to the friction in the cellular medium but the interactions with its molecular partners and microenvironment. To illustrate this subject further, we used the $V(R^2) - \overline{R^2}$ technique to analyze the statistics of single-molecule trajectories, specifically focusing on the slow diffusion of EGFR.

For live HeLa cells at rest, the $V(R^2) - \overline{R^2}$ plot of measured tracks of unliganded Qdot525-Ab-EGFR are presented in **Figure 9a**. In this plot, peak 2 was the most populated and stable state

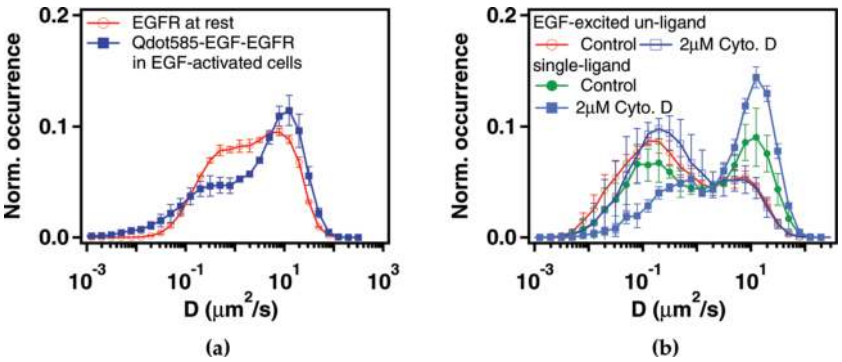

Figure 8 (a) Histogram of the diffusion coefficient of unliganded EGFR (open red circles) in the cells at rest and the liganded EGFR (solid blue squares) in EGF-activated cells. (b) Histogram of the diffusion coefficient of unliganded EGFR (open symbols) and the singly liganded species (filled symbols) on activated HeLa cells without (circles) or with (squares) Cytochalasin D pretreatment.

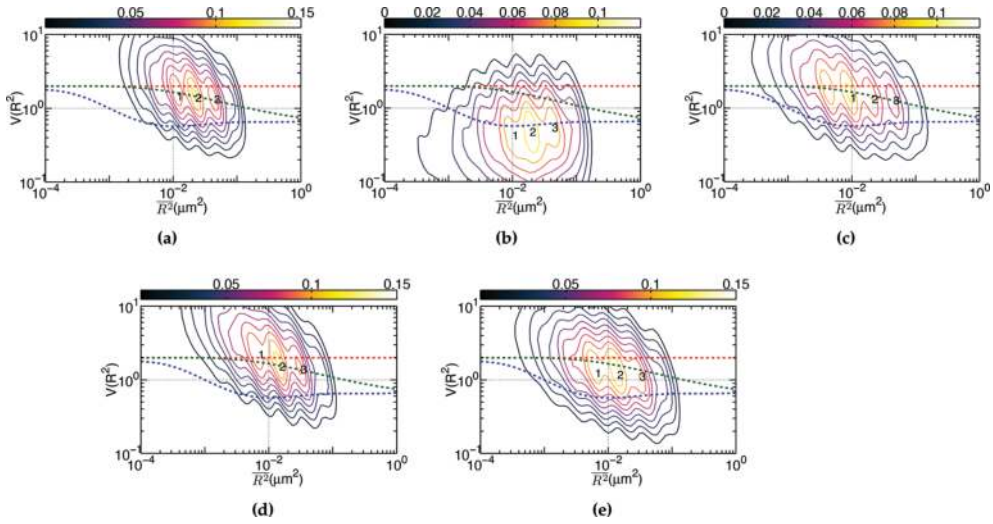

Figure 9 (a) The plot of $V(R^2) - \overline{R^2}$ for unliganded Qdot525-Ab-EGFR on live HeLa cells at rest. Simulated curves of the peak positions for receptor molecules under free Brownian motion (red dash line), diffusive motion with the confinement from actin corrals alone (green dash line), or both the actin corrals and lipid raft domains (blue dash line) are included for comparison. The same plot is shown for liganded Qdot585-EGF-EGFR in (b) EGF-activated cells, and (c) activated cells pretreated with nystatin. (d) Unliganded Qdot525-Ab-EGFR on live EGF-activated HeLa cells. (e) the same plot as (d) for unliganded Qdot525-Ab-EGFR on activated cells pretreated with nystatin. (a–c) have been reproduced from ref. [31].

among the three peaks detected, located at the $\left(\overline{R^2}, V(R^2)\right)$ coordinates of (0.01, 1.45), (0.02, 1.39), and (0.04, 1.33), respectively. Three simulated curves were plotted for proteins under free Brownian motion (red dash line), confinement by actin corrals alone (green dash line) or by both actin corrals and lipid domains (blue dash curves) and presented in **Figure 9a** for comparison. The peak positions of the three states clearly fell on the curve of the actin confinement, indicating that these unliganded receptor molecules were not free diffusers, but instead confined by the actin corrals alone.

With the EGFR at rest as the control, we proceeded to examine the diffusion of liganded Qdot585-EGF-EGFR. **Figure 9b** shows the $V(R^2) - \overline{R^2}$ plot of the liganded EGFR on activated HeLa cells. Three peaks were found at (0.01, 0.42), (0.02, 0.47), and (0.04, 0.54). These peak positions agreed better with the model that included the confinement effects of actin corrals and lipid raft domains. We used nystatin on the cells to sequester the membrane cholesterol and disrupt the lipid raft domains. **Figure 9c** displays the $V(R^2) - \overline{R^2}$ plot of the liganded EGFR on EGF-activated cells pretreated by nystatin. The three peaks of **Figure 9c**, at (0.01, 1.39), (0.02, 1.33), and (0.04, 1.28), fell again on the curve for the actin confinement model.

For unliganded Qdot525-Ab-EGFR on EGF-activated cells, the corresponding $V(R^2) - \overline{R^2}$ plot is presented in **Figure 9d**. Although peak 1 appeared to be produced by the free diffusion proteins, peaks 2 and 3 agree with the confinement model of the actin corrals alone. Qdot525-Ab-EGFR on the nystatin-pretreated cells (shown in **Figure 9e**) revealed similar

peaks at (0.006, 1.24), (0.014, 1.18), and (0.031,1.12), suggesting that lipid raft domains on activated cells play a minor role in restraining the motion of unliganded Qdot525-Ab-EGFR.

We proposed the following picture to explain our experimental results: Unliganded EGFRs at rest may locate outside the cholesterol-enriched lipid domains. EGF binding causes the receptors to move into the cholesterol-enriched lipid domains. Pretreatment of cells with nystatin, which can disrupt these lipid domains, results in local environmental changes of the ligand-bound EGFR. This interpretation is further supported by the observations shown in **Figure 9d** and **e** in which nystatin pretreatment did not alter the peak positions of unliganded EGFR on EGF-activated cells.

The $V(R^2)$ peak values of unliganded EGFRs in native cells at rest were near the free diffusion limit (**Figure 9a**). However, those unliganded species could have higher $V(R^2)$ peak values in highly EGF-activated cells due to much stronger confinements from EGF-promoted actin polymerization [30]. EGF ligation reduced the $V(R^2)$ values of Qdot585-EGF-EGFR to below the free diffusion limit (**Figure 9b**) due to the dressing effect by the lipid domain. These experimental findings were verified in three cell lines; including two cancer cell lines (HeLa and A431) and one non-tumorigenic breast epithelial cell line (MCF12A). These cell lines possess a wide range of EGFR expression levels and concentrations of membrane cholesterol. Therefore, the experimental results may represent a general behavior of unliganded and activated receptors in live cells.

4.2. Correlated motion of receptor proteins in plasma membrane of live cells

Receptor dimerization plays a critical role in initializing a signal cascade [48]. Do nearby receptor proteins move correlatively prior to dimer formation? Imagine when a receptor protein moves in the plasma membrane of a live cell, it may induce order in its surrounding lipid molecules through the protein-lipid interaction. A receptor protein and the induced lipid ordering can be viewed as a lipid-dressed protein. As two nearby proteins move in the plasma membrane, they may interact with each other through the ordered lipid molecules.

We can simulate the diffusive behaviors of two dressed proteins in proximity using coupled Langevin equations [49]. To display the mutual correlation between the two trajectories quantitatively, we expressed the position vectors as $\vec{x}_k(t) = A_k(t)e^{i\theta_k(t)}$, and defined the degree of mutual correlation as

$$C(\tau) = \mathrm{Re}\left[\frac{\sum \vec{x}_1{}^*(t)\cdot\vec{x}_2(t+\tau)}{\sqrt{\sum\left|\vec{x}_1(t)\right|^2}\sqrt{\sum\left|\vec{x}_2(t)\right|^2}}\right] = \frac{\sum_t A_1(t)A_2(t+\tau)\cos\left[\theta_2(t+\tau)-\theta_1(t)\right]}{\sqrt{\sum_t {A_1}^2}\sqrt{\sum_t {A_2}^2}}. \quad (6)$$

The summations were taken over a time mesh along the single-molecule tracks. By using this approach, we simulated the correlated motion of two Brownian-like particles with their spatial separation perturbed by a correlated thermal fluctuation [49]. We carried out the simulations from an initial condition that positioned one receptor at $\vec{x}_1 = (0,0)$ and places the other randomly within a 1-μm radius circle centered at (0,0). The coupled Langevin equations were

then solved to generate a pair of trajectories, and the degree of mutual correlation was calculated using Eq. (6). **Figure 10a** and **b** display the histograms of simulated trajectories with mutual correlations of 0 and 0.5, respectively. **Figure 10c** illustrates the histogram of correlation in experimental single-molecule tracks of paired Qdot525-Ab-EGFR and Qdot585-EGF-EGFR on live HeLa cells. As shown, the tracks clearly exhibited a correlation peak at 0.5.

By using this method, we were able to select those highly correlated segments from the single-molecule tracks and analyzed the correlated motion [31]. We plotted the $V(R^2) - \overline{R^2}$ plot of the motion of the unliganded Qdot525-Ab-EGFR correlated with liganded Qdot585-EGF-EGFR in **Figure 11a**. As the unliganded Qdot525-Ab-EGFR moved correlatively with a nearby liganded Qdot585-EGF-EGFR, the diffusion motility $\overline{R^2}$ of state 1 decreased drastically to near 10^{-3}, accompanied by a reduction of $V(R^2)$ to 0.1. It is interesting to note that the $V(R^2) - \overline{R^2}$ plot of the reverse case (i.e., Qdot585-EGF-EGFR relative to Qdot525-Ab-EGFR) differed in $\overline{R^2}$ (**Figure 11b**). The resident time of the liganded EGFR in state 2 became longer, and the $V(R^2)$ of both states 1 and 2 increased to 1, indicating that the liganded and unliganded EGFR resided in different lipid environments.

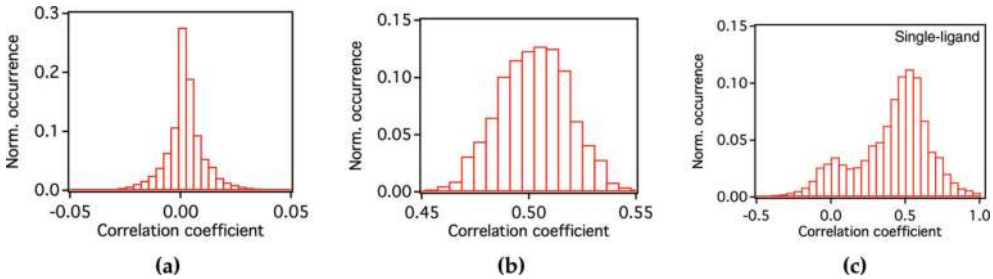

Figure 10 Histogram of the degree of correlation in simulated trajectories of (a) independent ($C(\tau) = 0$) or (b) correlated ($C(\tau) = 0.5$) diffusing particles. (c) Histogram of the degree of correlation existing in experimental trajectories of unliganded Qdot525-Ab-EGFR and liganded Qdot585-EGF-EGFR.

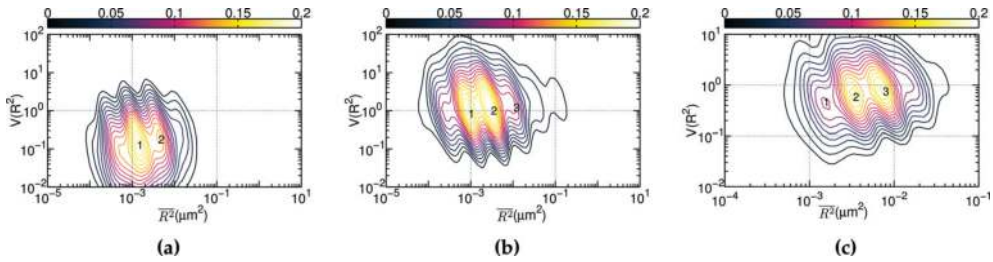

Figure 11 $V(R^2) - \overline{R^2}$ plot of correlated motion of dual EGFRs. (a) Unliganded Qdot525-Ab-EGFR correlatively moving with a nearby liganded Qdot585-EGF-EGFR companion, (b) liganded Qdot585-EGF-EGFR correlatively moving with a nearby unliganded Qdot525-Ab-EGFR, and (c) correlated motion of dual liganded EGFRs. This figure has been reproduced from ref. [31].

The $V(R^2) - \overline{R^2}$ plot of the correlated motion between two liganded EGFRs is presented in **Figure 11C**. Compared to the plot shown in **Figure 11b**, the $V(R^2)$ values of the two major states were decreased when the unliganded companion of **Figure 11b** was replaced by the liganded EGFR, perhaps because the lipid raft domains surrounding the two receptor molecules merged and yielded a larger dressing force during the highly correlated motion.

4.3. Cholesterol-mediated interaction between liganded EGF receptors

Ligand binding promotes receptor dimerization and leads to a downstream signaling cascade. Researchers have increasingly determined that lipid domains rich in raft sphingolipids (GM1) and cholesterol can facilitate signaling receptors to form a dimer [50–52]. The recent identification of cholesterol-dependent nanoassemblies with biophysical techniques also suggests that a cholesterol-mediated interaction exists between lipid domains to affect the organization, stability, and function of membrane receptor proteins [52–54].

We selected and analyzed those highly correlated segments from single-molecule trajectories to reveal the influence of cholesterol-mediated interactions [39]. **Figure 12** displays the $V\left(\overline{R_\tau^2}\right)$-$\overline{R_\tau^2}$ plots of paired Qdot585-EGF-EGFRs in three different cell lines. The contour plots are more scattered, indicating that these data are indeed highly sensitive to receptor interaction.

The $V\left(\overline{R_\tau^2}\right)$ value of the correlated Qdot585-EGF-EGFRs is considerably lower in A431 cells, which may be attributed to effective receptor-lipid and receptor-receptor interactions in these cells [33, 34]. To inspect the nature of the interactions and their relevance to receptor-induced lipid ordering, we again took advantages of the drug effects of nystatin and MβCD. **Figure 12b and c** display the $V\left(\overline{R_\tau^2}\right)$-$\overline{R_\tau^2}$ plots for the three cell lines pretreated with nystatin and MβCD. Correlated Qdot585-EGF-EGFRs appeared to have a weaker interaction in the nystatin-treated A431 cells as evidenced by an increased $V\left(\overline{R_\tau^2}\right)$ value. This observation may be explained by a

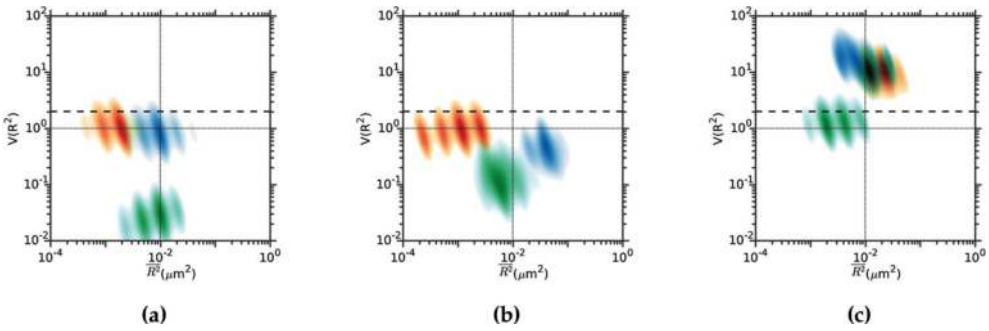

Figure 12 $V\left(\overline{R_\tau^2}\right)$-$\overline{R_\tau^2}$ plots of correlated Qdot585-EGF-EGFRs diffusing in the plasma membrane of (a) native cells, (b) nystatin-pretreated cells, and (c) MβCD-pretreated cells. Trajectory segments with a degree of correlation exceeding 0.8 were selected for analysis. Data are shown in red for HeLa cells, green for A431 cells, and blue for MCF12A cells. This figure has been reproduced from ref. [39].

less stable lipid domain due to a lower amount of cholesterol, which resulted in a larger variance in the diffusing step size of the correlated receptors. In contrast, the interaction became stronger in nystatin-treated MCF-12A cells, suggesting the effect of the cholesterol-mediated interaction was opposite to that of the receptor-lipid interaction. The $V\left(\overline{R_\tau^2}\right)$ of correlated Qdot585-EGF-EGFR in A431 increased by two orders of magnitude from 10^{-2} for native cells to 1 for MβCD treated cells. Of note, the $V\left(\overline{R_\tau^2}\right)$ value could be increased to higher than 10 in MβCD treated HeLa and MCF-12A cells, which suggests that a deterministic interaction dominated because the screening effect from the membrane cholesterol was reduced after membrane cholesterol was depleted. These results identified a vital role for membrane cholesterol in mediating the interaction between liganded receptors in the three cell lines.

4.4. Nonraft lipids and sphingolipids in live plasma membranes segregate into separated nanodomains

Previous data analysis implicitly assumed the coexistence of different lipid phases in plasma membranes. Indeed, lipid–lipid interactions were capable of inducing liquid ordered (Lo)-liquid disordered (Ld) phase coexistence in model lipid membranes [55, 56]. It was conjectured that plasma membrane composition is poised for selective and functional raft clustering at physiological temperatures [57]. However, such lipid nanodomains have remained largely unresolved in the plasma membrane of living cells. Researchers recently used a fluorescence correlation technique to successfully distinguish between free and anomalous molecular diffusion in a 30-nm focal spot of a stimulated emission depletion (STED) nanoscope [58]. The observed differences were attributed to transient cholesterol-assisted and cytoskeleton-dependent binding of sphingolipids to other membrane constituents. However, the optical force acting on the highly excited lipid molecules by the STED spot may not be negligible.

In our current study, we investigated lipid nanodomains in live plasma membranes at a much lower excitation level with light-sheet microscopy. We probed the nonraft lipids in living HeLa cells with carbocyanine dyes 1,1′-didodecyl- 3,3,3′,3′-tetramethylindocarbocyanine perchlorate (DiI-C12), which serves as an excellent lipophilic fluorescent probe with a strong partition tendency into the Ld phase [59]. The preference originated from the fact that highly packed lipids in Lo phase usually exclude exogenous molecules. BODIPY FL C_5-ganglioside GM_1 (BODIPY C_5-GM1) from ThermoFisher Scientific was used as a direct indication of lipid rafts. By synchronously adjusting the light-sheet position and the focal plane of the high NA objective lens, we were alble to acquire a 3D image of DiI-C12 and BODIPY C_5-GM1 in a living HeLa cell. **Figure 13a** displays a typical image of the scan with DiI-C12 shown in blue and BODIPY C_5-GM1 in orange. The 3D point spread function (PSF) of the light-sheet microscope was deduced (shown in **Figure 13b**) using a fluorescent bead with a diameter of 100 nm. We exploited this PSF to deconvolve the image [60] of DiI-C12 and BODIPY C_5-GM1. The resulting deconvolved image is shown in **Figure 13a**.

Following the formalism developed by Veatch et al. [61], we calculated both the auto-correlation function $A(r) = \langle \rho(R)\rho(R-r)\rangle / \langle \rho(r)\rangle^2$ and the cross-correlation function $C(r) = \langle \rho_1(R)\rho_2(R-r)\rangle / (\langle \rho_1(r)\rangle \langle \rho_2(r)\rangle)$ of DiI-C12 and BODIPY C_5-GM1. The results are presented in **Figure 14**, which indicates that both species may form clusters with an average diameter of less than 150 nm.

http://dx.doi.org/10.5772/intechopen.72858

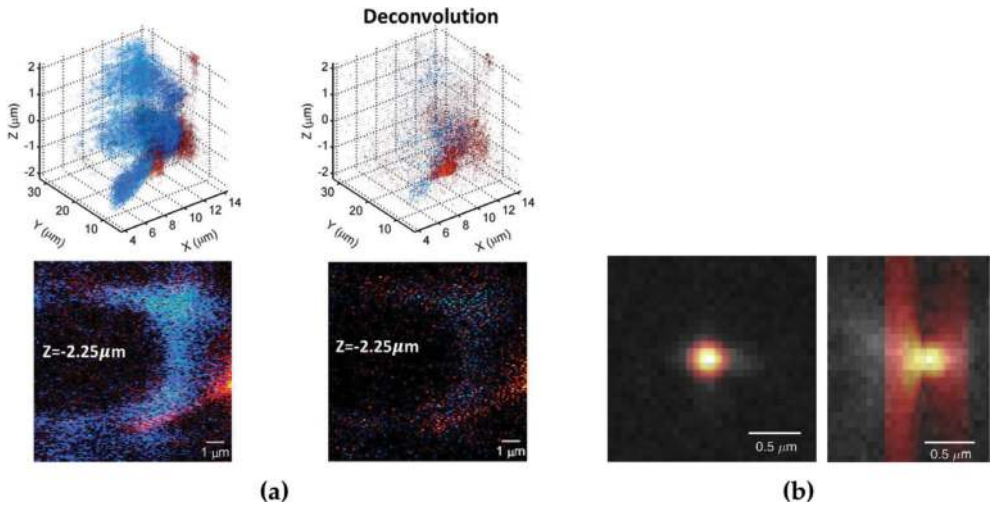

Figure 13 (a) 3D fluorescence distribution (left) and its deconvoluted image (right) from DiI-C12 (blue) and BODIPY C_5-GM1 (orange) fluorophores in a living HeLa cell. The cross section ($z = -2.25$ μm) of the distribution was shown below. (b)the point spread function of the light-sheet microscope on the xy- (left) and xz-plane (right) emitted from a fluorescent bead with a diameter of 100 nm.

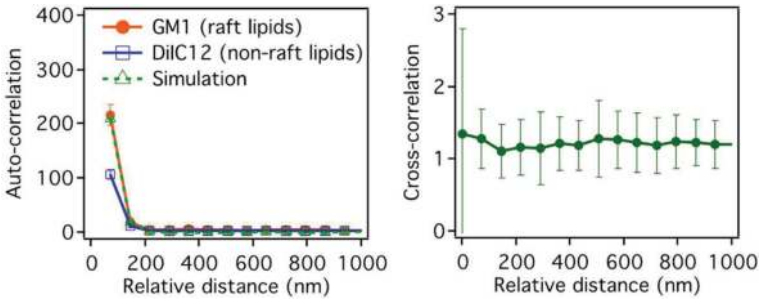

Figure 14 The auto-(left) and cross-(right) correlation function of DiI-C12 and BODIPY C_5-GM1 calculated from the deconvoluted image of **Figure 13a**.

To retrieve information about the lipid clustering process from the measured pair correlation, we simulated lipid clustering dynamics. First, we randomly distributed M clusters in an imaging region with each cluster containing N molecules in a circle with diameter R. **Figure 15a** illustrates an example of two randomly distributed clusters (M = 2) at a spatial resolution of 2 nm. We then binned the molecules in a cluster to the pixel size of the camera used (see **Figure 15b**). By using these cluster images, we calculated the auto- and cross-correlation functions with three different lipid clustering models: 1) a random clustering model, 2) an aggregation model, and 3) a segregation model. The random clustering model assumed that two lipid species were independently and randomly distributed in an area. In contrast, the lipid molecules in the aggregation and segregation models were stochastically distributed in each cluster with a Gaussian distribution. There is a major difference between

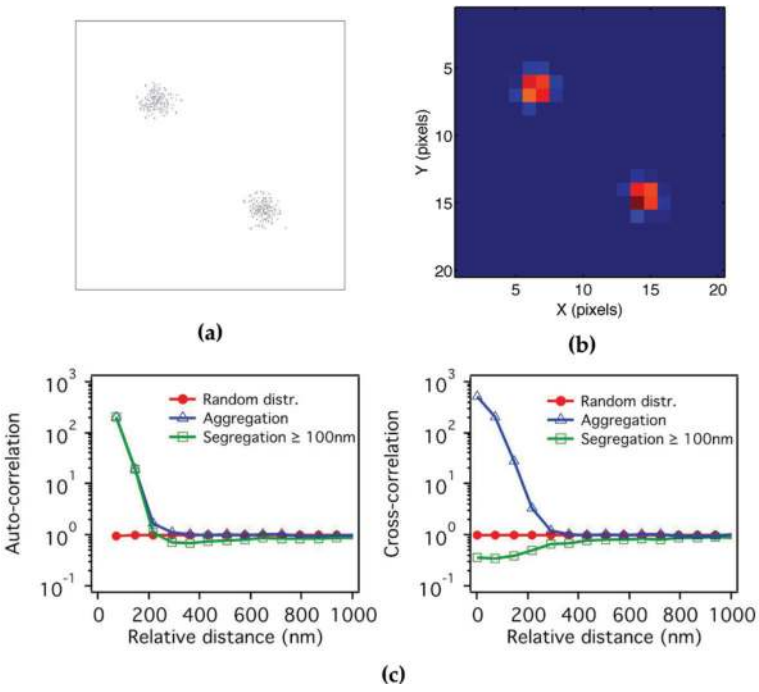

Figure 15 (a) Two randomly distributed clusters (M = 2) at a spatial resolution of 2 nm was prepared in a simulation area, (b) the two clusters were binned to the pixel size of the camera used. (c) the auto- (left) and cross- (right) correlation function using the parameters: R = 72 nm, N = 100, and M = 100 (2.8 clusters/μm^2) were simulated with the random clustering model (filled circles), aggregation model (open triangles), and segregation model (open squares).

the latter two models. In the aggregation model, any two clusters will attract each other to form an overlapping cluster with the same center of mass (but with different radii). In the segregation model, two clusters will experience a repulsive force to yield the minimum separation distance Δ. To simulate the segregation process, we first used a random number generator to produce the center position X_1 of one cluster and then used the multiplicative congruential generation algorithm to position the other cluster to lie in the interval of $[0,\ X_1 - \Delta)$ or $(X_1 + \Delta,\ 1]$. In this way, the second cluster was located randomly but was excluded from the neighborhood of X_1 with a minimum separation Δ. For a fair comparison, we kept the number of clusters, cluster size, and number of molecules in each cluster at the same values. **Figure 15** shows the simulation results for the following parameters: the waist size of the cluster was 72 nm, the number of molecules in a cluster was 100, and the number of clusters in an image was 100 (i.e., 2.8 clusters/μm^2), which yielded the short-distance auto-correlation and agreed well with the experimental result shown in **Figure 14**.

By comparing **Figure 15c** with **Figure 14**, we concluded that our data could not fit to the model of random clustering. From the comparison of cross-correlation shown in **Figures 15c** and **14**, we could remove the aggregation model, and we concluded that our data was better described by the segregation model with a segregation distance <100 nm.

It was discovered that the raft lipid species GM1 can be tightened by pentameric cholera toxin-β (CTxB), which initiates a minimum raft coalescence to form the GM1 nanodomains [62]. The plasma membranes in our study were in their native state without perturbations from either intense laser spot or cross linking reagent. Thus, our evidence for segregation of nonraft lipids and GM1 into separate nanodomains supports the idea that such a phase coexistence in a native plasma membrane not only exists but also is a general behavior of living cells.

4.5. Probing translocation of HIV-1 tat peptides in living cells with tat-conjugated quantum dot nanosensors

Viral infection can initiate at entry points on plasma membranes via lipid domains. Drug delivery may benefit from our understanding of this entry process because upon arriving at target tissues, drug molecules must also cross the plasma membrane to reach the sites of action. It is of particular interest to make drug molecules that cross cellular membranes directly to avoid the complications of vesicle-mediated internalization pathways. Recently, cell-penetrating peptides (CPPs), which are short sequences (8 to 30) of amino acids (aa) with a net positive charge in water [63], were found to exhibit such a membrane-crossing capability. An 11 aa segment in the trans activator of a transcription protein of the human immunodeficiency virus is a prototypical example of a CPP that can effectively penetrate a cell [64, 65]. The interactions involved in the approach to developing a TatP-coated nanoscale probe may determine whether the uptake of the probe succeeds or fails. To illustrate the potential of biomolecule-conjugated QDs as a cellular dynamic probe, in this section we briefly discuss the results of the translocation of TatP-conjugated QDs across the plasma membranes of live cells using the single-molecule tracking technique [17].

The first step for cellular internalization may involve some form of interaction between the Tat peptides and the surface of the cell. The strong anionic charge present on the glycosaminoglycan (GAG) chains of the proteoglycans (PGs) makes them favorable first-binding sites for the cationic Tat peptides [20, 66, 67]. To verify this scenario, we treated cells with Heparinase III enzyme (HSase) to cleave heparan sulfate (HS) groups from heparan sulfate proteoglycans (HSPGs). We observed a reduction in TatP-QD internalization of 74% at 30 min. Treatment with Cyto D, which can inhibit actin polymerization and thereby disrupt the cellular actin framework [68], resulted in a similar drop in TatP-QD internalization. The results indicate that both HS-mediated binding and the interaction with intracellular actin filaments are crucial for the rapid intake of TatP-QDs.

4.5.1. TatP-QDs approaching cell surface aggregate at selected regions of plasma membrane

For single-particle tracking, we prepared a cell culture medium containing 1 μm free TatPs and 1 nM TatP-QD nanosensors. The major species of free TatPs were used to restructure the environment of the membrane-peptide interaction, whereas TatP-QDs served as nanoscale dynamic pens to depict the landscape of the membrane-peptide interaction. We conducted single-particle trajectory analysis of the TatP-QDs with light-sheet microscopy to reveal the translocation dynamics. A unique affordance of our light-sheet microscope was the ability to track TatP-QDs in parallel, providing a global view of the dynamics of the approaching TatP-QDs. However, due to the

limited image-taking speed of the camera used, we were only able to track TatP-QDs within a short distance from the cell surface.

Without external interaction, these Tat-QD nanosensors were expected to traverse the extracellular space through a random walk search, attach to the membrane, and then diffuse to find a suitable entrance site. **Figure 16a** displays three trajectories of TatP-QDs, color-coded to indicate the approaching times. The green surface depicts the cell surface rendered from the phase contrast images taken by scanning the imaging focal plane at different z positions in the cell. The determination of the cell profile was limited by the diffraction effect of the objective lens used, yielding a resolution of 200 nm in the lateral plane and 500 nm in the axial direction. As indicated in the top inset, the initial approaching trajectories of some of the Tat-QDs resembled directed movement under a force field, and the motion became more diffuse as the TatP-QDs come closer to the cell surface. A longer observation period accumulated more approaching events and revealed the trajectory aggregates at selected regions of the plasma membrane (**Figure 16b**).

The binding affinity of TatP for HSPGs was greater than that for anionic lipids by 2 to 3 orders of magnitude. Given that the anionic HSPG chains on the plasma membrane [20, 69, 70] may be favorable binding sites for cationic CPPs, we hypothesized that the trajectory aggregates were caused by HS groups in the HSPG chains. To verify this hypothesis, we treated the cells with HSase to cleave the HS groups from the HSPGs, which revealed considerably fewer and more randomly positioned spots in the extracellular space. Thus, the observed trajectory aggregation seems to be caused by the binding to HS groups on the membranes and suggests that HSPGs play a critical role in redirecting the TatP entry process toward spatially restricted sites on the plasma membrane.

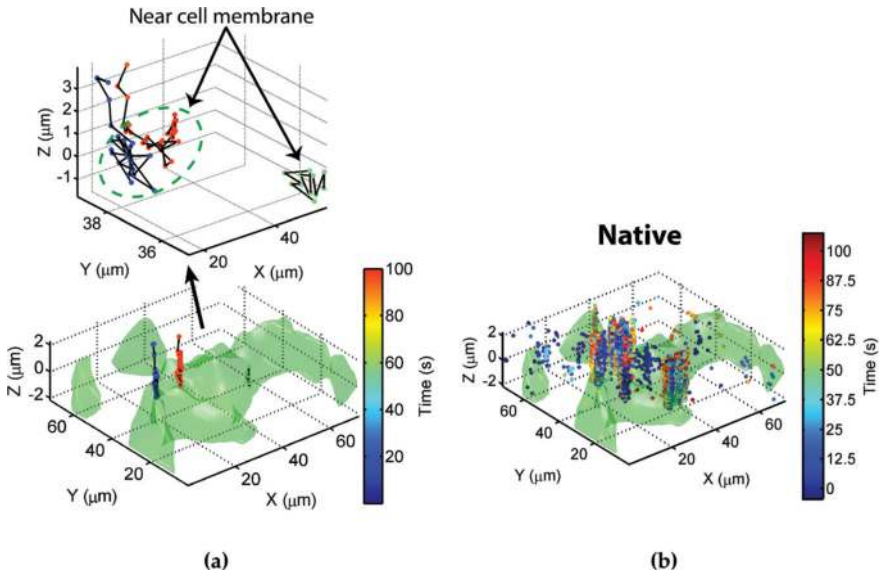

Figure 16 (a) Three trajectories of TatP-QDs near a living HeLa cell (green) were color-coded to indicate their appearing times. The green profile denotes the cellular surface rendered from optical sectioning phase contrast images; (b) when duration was increased to acquire information on more approaching events, trajectory aggregates were observed at selected regions on a native HeLa cell. This figure has been reproduced from ref. [17].

4.5.2. Spectral-embedding analysis of trajectory aggregates of TatP-QDs

As TatP-QDs translocate across the plasma membrane of a living cell, the probing particles can record the influences of the cellular environment on their trajectories. We considered the trajectory $\vec{r}\ (t)$ to be produced by a stochastic process with influences on the probing particle by its local environment, which may have different realizations with the corresponding interaction potentials $U_i\left(\vec{r} - \vec{\xi}\right);\ \ i = 1, .., n$. Thus, the trajectory coordinates of the nanosensors could implicitly record the configurations of the local environment. Recently, Wang and Ferguson generated a reconstruction of single-molecule free-energy surfaces from time-series data of a physical observable by using the generalized Takens Delay Embedding Theorem [34]. Here we focused on retrieving the eigenmodes of the trajectory coordinates of TatP-QDs to identify the mechanism underlying the trajectory aggregation of TatP-QDs.

We used the spectral-embedding technique [35] to extract a low-dimensional manifold from a set of trajectories: $\vec{r}_i(t); i = 1, .., n$. A graph-based method provided a useful discretized approximation of the manifold [36] and enabled an efficient construction of the eigendecomposition. The first eigenvector we retrieved was trivial with the corresponding eigenvalue giving only the data density in a cluster. We then focused on the next two eigenvectors, ϕ_2 and ϕ_3, which offered the most critical information on the interactions between TatP-QDs and their cellular environments.

Figure 17 presents two trajectory aggregates of the TatP-QDs: one (left) is near a living cell, and the other (right) is directly on top of the cell surface. All of the coordinates of the trajectory aggregates are shown in gray. The location coordinates of the TatP-QDs associated with the left

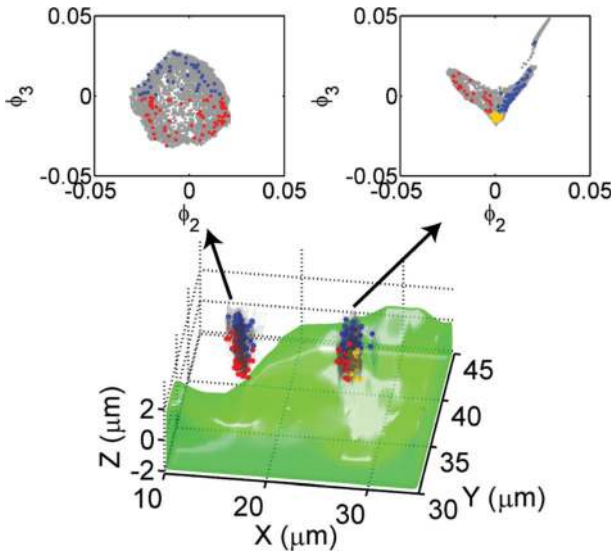

Figure 17 Two trajectory clusters (gray) of TatP-QDs near a living HeLa cell (green) are presented on a manifold of spectral-embedding eigenvectors (top inset). For each trajectory cluster, the $\left[V\left(\overline{R_\tau{}^2}\right)\right]$-$\left[\overline{R_\tau(t)}\right]^2$ coordinates of the trajectory segments within 2% variance of the peak shown in **Figure 18** are displayed in blue on the far side, red near the $z = 0$ plane, and yellow for those closest to the cell membrane. This figure has been reproduced from ref. [17].

cluster present a nearly circular distribution on the ϕ_2-ϕ_3 plane. The right cluster, however, displays a V-shaped distribution. Our results indicate that the spectrally decomposed structure of the trajectory aggregates provides the information on the interaction of the TatP-QDs with their cellular environments.

4.5.3. Influence of actin framework on translocation of TatP-QDs

The findings of a recent study indicated that on attachment to a membrane surface, Tat peptides can remodel the actin framework in an actin-encapsulated giant unilamellar vesicles (GUV) [69]. However, it remains unclear whether such multiplexed membrane and cytoskeletal interactions can also occur in a living cell. The trajectories of nanoscale probing particles may provide the answer. To extract relevant stochastic and geometrical structures from the data and gain insights into the mechanism that generated the data, we generated the $V\left(\overline{R_\tau^2}\right)$-$\overline{R_\tau^2}$ plots of the trajectories in **Figure 18**, which summarizes the single-particle diffusion statistics from 23,382 TatP-QD trajectories.

A single peak at the coordinates (0.15, 0.21), which is well below the free diffusion limit of $V\left(\overline{R_\tau^2}\right) = 2$, is shown in **Figure 18a**, suggesting that the TatP-QDs did not diffuse freely near a native HeLa cell. The peak split into two and shifted downward to $V\left(\overline{R_\tau^2}\right) = 0.06$ for Cyto D-treated cells (**Figure 18b**), indicating that TatP-QDs experience a stronger interaction with a strained cellular membrane. This finding is understandable because, without the support of an actin framework, the plasma membrane may develop a higher local curvature as a result of TatP-QD attachment. In native cells, the effect of the interaction between Tat peptides and the cell membrane may be counter balanced by that of the Tat and actin filaments, resulting in a higher $V\left(\overline{R_\tau^2}\right)$.

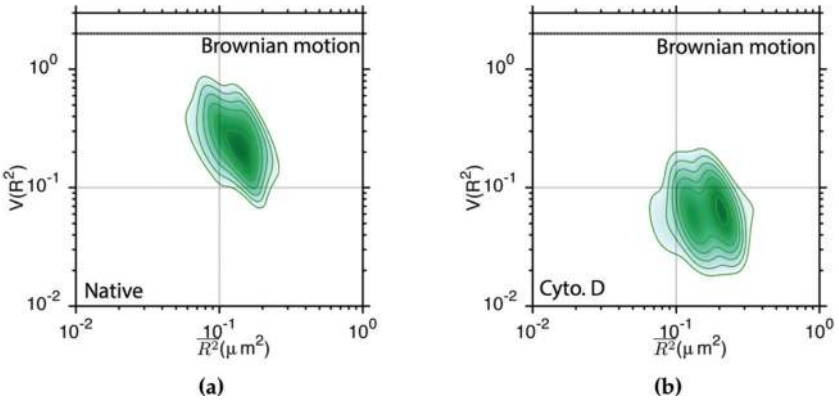

Figure 18 2D contour plot of $\left[V\left(\overline{R_\tau^2}\right)\right]$-$\overline{[R_\tau(t)]^2}$ histogram for TatP-QDs moving in the neighborhood of (a) living HeLa cell and (b) Cyto D-pretreated cell. This figure has been reproduced from ref. [17].

We also analyzed each trajectory aggregate by selecting segments that fell within 2% variance of the $\left[V\left(\overline{R_\tau{}^2}\right)\right]$-$\overline{[R_\tau(t)]^2}$ peak. Labeling the resulting $\left[V\left(\overline{R_\tau{}^2}\right)\right]$-$\overline{[R_\tau(t)]^2}$ coordinates on the trajectories offered insight into the environmental influences on the TatP-QDs. For example in the left trajectory cluster of **Figure 17**, these special points are shown in blue on the far side and red near the z = 0 plane. The blue dots were uniformly distributed at the rim of the circle on the ϕ_2-ϕ_3 plane, and the distribution of the red dots, which were close to the cell membrane, appeared to be denser on the $\phi_2 > 0$ side. In the trajectory aggregate directly on top of the cell, the blue dots were located at the right leg ($\phi_2 > 0$) and the red points dots were concentrated at the left leg ($\phi_2 < 0$) of a V-shaped distribution. Yellow dots, which represent trajectory segments closest to the cell membrane, aggregated at the tip of the V-shaped distribution, suggesting the formation of hot spots of interaction on the cell membrane, which may be supported by specifically oriented actin filaments.

4.5.4. Classification of TatP-QD trajectories

We also applied spectral embedding [17, 70] to classify 23,382 TatP-QD trajectories measured on 30 cells. In **Figure 19**, the resulting circular or V-shaped distributions on the ϕ_2-ϕ_3 plane are displayed in green. For classification, the norm of the residuals, defined as the sum of the squared deviation from the circular distribution of free diffusion, was used as the metric. The coordinates (blue) within 2% variance of the $\left[V\left(\overline{R_\tau{}^2}\right)\right]$-$\overline{[R_\tau(t)]^2}$ peak with the corresponding contours were also included for comparison. As shown in **Figure 20**, the class of circular

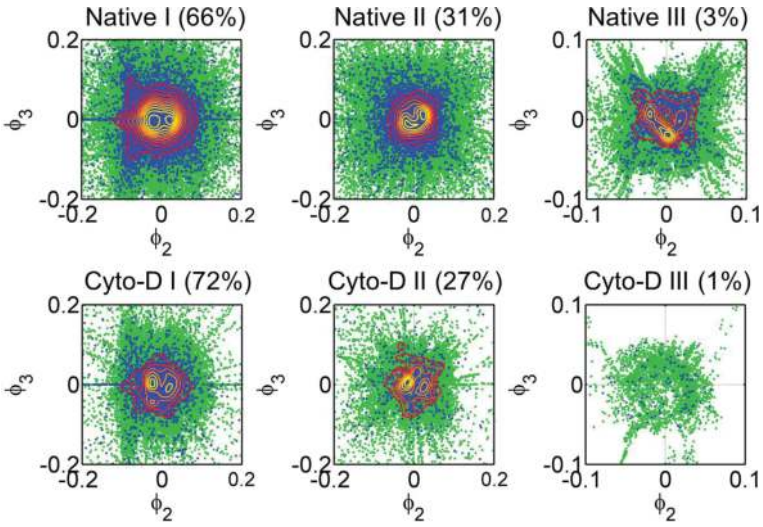

Figure 19 Spectral embedding manifold plots (green in insets) of 23,382 trajectories of TatP-QDs measured on 30 living HeLa cells (up row) and 5112 trajectories measured on Cyto D-treated cells (bottom row). The $\left[V\left(\overline{R_\tau{}^2}\right)\right]$-$\overline{[R_\tau(t)]^2}$ coordinates of the trajectory segments within 2% variance of the peaks shown in **Figure 18** are displayed in blue, with associated contour curves revealing the peak profiles. This figure has been reproduced from ref. [17].

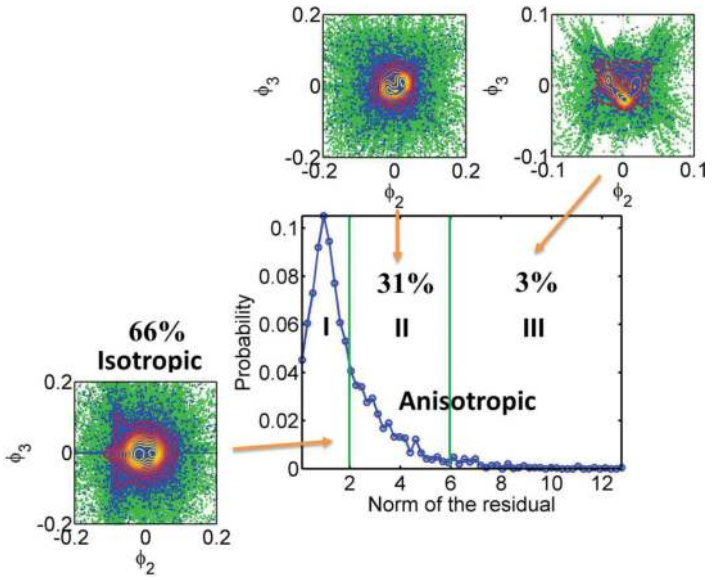

Figure 20 Classification (center) of spectral embedding manifold plots (green in insets) of 23,382 trajectories of TatP-QDs measured on 30 living HeLa cells. The $\left[V\left(\overline{R_\tau{}^2}\right)\right]$-$\overline{[R_\tau(t)]^2}$ coordinates of the trajectory segments within 2% variance of the peaks shown in **Figure 18** are displayed in blue, with associated contour curves revealing the peak profiles. This figure has been reproduced from ref. [17].

distribution with a norm of the residuals of 0.91 ± 0.34 contained about 66% of the data from the native cells. The moderate (2 to 6) and highly anisotropic (>6) trajectory data occupied 31 and 3%, respectively. We acquired 5112 trajectories for the Cyto D-treated cells. The proportions of the moderate and highly anisotropic trajectories decreased to 27 and 1%, respectively. Treatment with Cyto D reduced the cellular uptake of the TatP-QDs to 25% of that of the native cells, indicating that both the isotropic and moderate anisotropic classes played a minor role in the initial cellular uptake. The trajectories belonging to the highly anisotropic class resulted in 75% uptake. These findings indicate the formation of funnel passages for the TatP-QDs due to the combined effect of HS-binding and actin remodeling.

5. Conclusion

Probing the distribution and mobility of proteins in live cellular environments is crucial for understanding cellular functions and regulatory mechanisms, which also serve as the basis for developing therapeutic strategies. Factors that affect protein mobility are difficult to reconstitute in vitro using purified constituents. Single-molecule imaging and tracking provide direct access to probe the properties of molecular assemblies and the kinetics of the interaction in live cellular environments. However, biological media are spatially inhomogeneous, which is poorly conveyed by measuring just a few, sparse single-molecule trajectories. Finding a way to efficiently and reliably extract useful information from a large amount of trajectory data is an obstacle of this technique.

A biomolecule subjected to random influences can explore its possible outcomes and evolves to yield a dispersion over its state space. The evolution may contain both contributions from deterministic and stochastic forces. To provide high-quality statistics sampled by appropriate probing biomolecules while preserving single-molecule sensitivity, we developed a 2D analysis of single-molecule trajectories with $V\left(\overline{R_\tau^2}\right)$ and $\overline{R_\tau^2}$ (normalized variance-vs-MSD). Here the MSDs were used to quantify the diffusion of a protein in its cellular environment, and the normalized variance discloses the nature of these interactions. Thus, the plot can be more sensitive than MSD alone to reflect the diffusive dynamics of a protein in cellular environments. We applied this 2D analysis technique to the dimerization processes of EGFRs in live cells under varying cellular conditions. Based on this study, we found that unliganded species appear to remain outside the cholesterol-enriched lipid domains. After ligand binding, EGFR molecules may relocate to lipid raft domains. This experimental finding was verified using three cell lines with a wide range of EGFR expression levels and membrane cholesterol concentrations, suggesting that these results may represent a general behavior of unliganded and activated receptors in live cells. Reigada et al. recently applied near-field scanning optical microscopy to fixed monocytes and found that raftophilic proteins did not physically intermix at the nanoscale with CTxB-GM1 nanodomains but converged within a characteristic distance [62]. Our result of unliganded EGFR agrees with this finding but on live cells without CTxB tightening.

Selectively tagging EGFR species with semiconductor quantum dots allowed us to monitor the correlated motions of unliganded and liganded species. Paired liganded receptors, which diffused in proximity on the plasma membrane interacted with each other and caused the receptors to move correlatively. The correlated motions can be caused by the correlated fluctuations in the lipid environment, which occur when the two receptors are closely separated. The correlated motion can be changed by manipulating either the distribution or total quantity of the membrane cholesterol, suggesting that the membrane cholesterol plays a vital role in mediating the interactions between the liganded receptors. Our quantitative 2D analysis method can capture the dynamic receptor interactions at the single-molecule level, providing details that are often obscured in other methods.

We further used the HIV-1 Tat peptide-conjugated QD as a nanosensor to illustrate the translocation dynamics of the Tat peptides in living cells. By using spectral-embedding analysis, we extracted an intrinsic low-dimensional manifold, which was formed by the isotropic diffusion and a fraction of the directed movement, from the measured trajectories. Our result suggest that HSPGs play a significant role in redirecting the TatP-QD entry process toward spatially restricted sites on the plasma membrane. We further applied 2D analysis of $V\left(\overline{R_\tau^2}\right)$-$\overline{R_\tau^2}$ to determine the underlying cause of the trajectory aggregation. We found that the membrane deformation induced by the Tat-peptide attachment increased with the disruption of the actin framework, which resulted in higher interactions on the TatP-QDs. In native cells, the Tat peptides could remodel the actin framework to reduce their interaction with the local membrane environment.

Semiconductor quantum dots conjugated with appropriate peptides or antibodies are appealing for probing cellular dynamic events in living cells. The nanosensors have the advantages of high emission efficiency, wavelength tunability, and long-term stability, which have led to a variety of applications in cellular sensing and imaging. Biomolecule-conjugated QD nanosensors are also

useful for studying the interactions, stoichiometries, and conformational changes of proteins in living cells, which provides an understanding of the mode of the interaction and free-energy surfaces, and can reveal the stable states and dynamic pathways of biomolecules in live cells. The application examples presented in this chapter clearly support the use of biomolecule-conjugated QDs as probes for the cellular dynamics in living cells.

Acknowledgements

This research was funded by the Ministry of Science and Technology of the Republic of China (grant number MOST 106-2112-M-009-019-MY3). Parts of this chapter are taken from the authors' former work with permission of the Creative Commons Attribution license.

Conflicts of interest

The author declares that he has no competing interests.

Nomenclature

Ab	antibody
CPP	cell-penetrating peptide
CTxB	cholera toxin-β
cyto D	cytochalasin D
ETL	electrically tunable lens
FDT	fluctuation-dissipation theorems
GAG	glycosaminoglycan
GUV	giant unilamellar vesicles
HS	heparan sulfate
HSPG	heparan sulfate proteoglycan
MβCD	methyl β-cyclodextrin
MSD	mean square displacement
PG	proteoglycan
PMF	potential of mean force
PSF	point spread function
QD	quantum dot

sCMOS	complementary metal-oxide semiconductor
TatP	transactivator of transcription (Tat) peptide
TatP-QD	TatP-conjugated quantum dot

Author details

Jung Y. Huang

Address all correspondence to: jyhuang@faculty.nctu.edu.tw

Department of Photonics and The T.K.B. Research Center for Photonics, Chiao Tung University, Hsinchu, Taiwan

References

[1] Lippincott-Schwartz J, Snapp E, Kenworthy A. Studying protein dynamics in living cells. Nature Reviews Molecular Cell Biology. 2001;**2**:444-456

[2] Hung MC, Link W. Protein localization in disease and therapy. Journal of Cell Science. 2011;**124**:3381-3392

[3] Masson JB, Dionne P, Salvatico C, Renner M, Specht CG, Triller A, Dahan T. Mapping the energy and diffusion landscapes of membrane proteins at the cell surface using high-density single-molecule imaging and Bayesian inference: Application to the multiscale dynamics of glycine receptors in the neuronal membrane. Biophysical Journal. 2014;**106**:74-83

[4] Kusumi A, Tsunoyama TA, Hirosawa KM, Kasai RS, Fujiwara TK. Tracking single molecules at work in living cells. Biophysical Journal. 2014;**106**:74-83

[5] Liu Z, Lavis LD, Betzig E. Imaging live-cell dynamics and structure at the single-molecule level. Molecular Cell. 2015;**58**:644-659

[6] Serag MF, Abadi M, Habuchi S. Single-molecule diffusion and conformational dynamics by spatial integration of temporal fluctuations. Nature Communications. 2014;**5**:5123

[7] Michalet X. Mean square displacement analysis of single-particle trajectories with localization error: Brownian motion in an isotropic medium. Physical Review E. 2010;**82**:041914

[8] Medintz IL, Uyeda HT, Goldman ER, Mattoussi H. Quantum dot bioconjugates for imaging, labelling and sensing. Nature Materials. 2005;**4**:435-446

[9] Jaiswal JK, Simon SM. Imaging live cells using quantum dots. Cold Spring Harbor Protocols. 2015. p. doi:10.1101/pdb.top086322

[10] Zhang JJ, Zheng TT, Cheng FF, Zhang JR, Zhu JJ. Toward the early evaluation of therapeutic effects: An electrochemical platform for ultrasensitive detection of apoptotic cells. Analytical Chemistry. 2011;**83**:7902-7909

[11] Zhang JJ, Cheng FF, Li JJ, Zhu JJ, Lu Y. Fluorescent nanoprobes for sensing and imaging of metal ions: Recent advances and future perspectives. Nano Today. 2016;**11**:309-329

[12] Hana HS, Niemeyerb E, Huang Y, Kamoun WS, Martin JD, Bhaumik J, Chen Y, Roberge S, Cui J, Martin MR, Fukumura D, Jain RK, Bawendi MG, Duda DG. Quantum dot/antibody conjugates for in vivo cytometric imaging in mice. Proceedings of the National Academy of Sciences of the United States of America. 2015;**112**:1350-1355

[13] Wereszczynski J, McCammon JA. Statistical mechanics and molecular dynamics in evaluating thermodynamic properties of biomolecular recognition. Quarterly Reviews of Biophysics. 2012;**45**:1-25

[14] Seifert U. Stochastic thermodynamics, fluctuation theorems and molecular machines. Reports on Progress in Physics. 2012;**75**:126001-126058

[15] Singera A, Erban R, Kevrekidis IG, Coifman RR. Detecting intrinsic slow variables in stochastic dynamical systems by anisotropic diffusion maps. Proceedings of the National Academy of Sciences of the United States of America. 2009;**106**:16090-16095

[16] Coifman R, Kevrekidis I, Lafon S, Maggioni M, Nadler B. Diffusion maps, reduction coordinates and low dimensional representation of stochastic systems. SIAM Multiscale Model Simulation. 2008;**7**:842-864

[17] Lin CY, Huang JY, Lo LW. Depicting binding-mediated translocation of HIV-1 tat peptides in living cells with Nanoscale pens of tat-conjugated quantum dots. Sensors. 2017;**17**:315-314

[18] Welsher K, Yang H. Multi-resolution 3D visualization of the early stages of cellular uptake of peptide-coated nanoparticles. Nature Nanotechnology. 2014;**9**:198-203

[19] Belting M. Heparan sulfate proteoglycan as a plasma membrane carrier. Trends in Biochemical Sciences. 2003;**28**:145-151

[20] Yang J, Tsutsumi H, Furuta T, Sakurai M, Mihara H. Interaction of amphiphilic alpha-helical cell-penetrating peptides with heparan sulfate. Organic & Biomolecular Chemistry. 2014;**12**:4673-4681

[21] Gallavotti G, Cohen EGD. Dynamical ensembles in nonequilibrium statistical mechanics. Physical Review Letters. 1995;**74**:2694

[22] Kurchan J. Fluctuation theorem for stochastic dynamics. Journal of Physics A: Mathematical and General. 1998;**31**:3719

[23] Lebowitz JL, Spohn HA. Gallavotti-Cohen-type symmetry in the large deviation functional for stochastic dynamics. Journal of Statistical Physics. 1999;**95**:333

[24] Jarzynski C. Nonequilibrium equality for free energy differences. Physical Review Letters. 1997;**78**:2690

[25] Jarzynski C. Equilibrium free-energy differences from nonequilibrium measurements: A master-equation approach. Physical Review E. 1997;**56**:5018

[26] Crooks GE. Path-ensemble averages in systems driven far from equilibrium. Physical Review E. 2000;**61**:2361

[27] Hummer G, Szabo A. Free energy reconstruction from nonequilibrium single-molecule pulling experiments. Proceedings of the National Academy of Sciences of the United States of America. 2001;**98**:3658

[28] Hummer G, Szabo A. Time-reversal and entropy. Journal of Statistical Physics. 2003;**110**:269

[29] Zwanzig R. Nonequilibrium Statistical Mechanics. Oxford, UK: Oxford University Press; 2001

[30] Lin CY, Huang JY, Lo LW. Energetic modeling and single-molecule verification of dynamic regulation on receptor complexes by actin corrals and lipid raft domains. The Journal of Chemical Physics. 2014;**141**:215102

[31] Lin CYL, Huang JY, Lo LW. Unraveling the impact of lipid domains on the dimerization processes of single-molecule EGFRs of live cells. Biochimica et Biophysica Acta. 1848;**2015**: 886-893

[32] Tome T, de Oliveira MJ. Entropy production in irreversible systems described by a Fokker-Planck equation. Physical Review E. 2010;**82**:021120

[33] Jaynes E. The minimum entropy production principle. Annual Review of Physical Chemistry. 1980;**31**:579-601

[34] Wang J, Ferguson AL. Nonlinear reconstruction of single-molecule free-energy surfaces from univariate time series. Physical Review E. 2016;**93**:032412-032428

[35] Nadler B, Lafon S, Coifman RR, Kevrekidis IG. Diffusion maps, spectral clustering and reaction coordinates of dynamical systems. Applied and Computational Harmonic Analysis. 2006;**21**:113-132

[36] von Luxburg, U. A Tutorial on spectral clustering. Statistics and Computing. 2007;**174**:395–416

[37] Jaqaman K, Loerke D, Mettlen M, Kuwata H, Grinstein S, Schmid SL, Danuser G. Robust single-particle tracking in live-cell time-lapse sequences. Nature Methods. 2008;**5**:695-702

[38] Wu PH, Agarwal A, Hess H, Khargonekar PP, Tseng Y. Analysis of video-based microscopic particle trajectories using Kalman filtering. Biophysical Journal. 2010;**98**:2822-2830

[39] Lin CY, Huang JY, Lo LW. Exploring in vivo cholesterol-mediated interactions between activated EGF receptors in plasma membrane with single-molecule optical tracking. BMC Biophysics. 2016;**9**:1-11

[40] Kusumi A, Fujiwara TK, Morone N, Yoshida KJ, Chadda R, Xie M, Kasai RS, Suzuki KGN. Membrane mechanisms for signal transduction: The coupling of the meso-scale raft domains to membrane-skeleton-induced compartments and dynamic protein complexes. Seminars in cell and. Developmental Biology. 2012;**23**:126-144

[41] Balla T. Phosphoinositides: Tiny lipids with Giant impact on cell regulation. Physiological Reviews. 2013;**93**:1019-1137

[42] Jaqaman K, Grinstein S. Regulation from within: The cytoskeleton in transmembrane signaling. Trends in Cell Biology. 2012;**22**:515-526

[43] Iyengar G, Rao M. A cellular solution to an information-processing problem. Proceedings of the National Academy of Sciences of the United States of America. 2014;**111**:12402-12407

[44] Gschwind A, Fischer OM, Ullrich A. The discovery of receptor tyrosine kinases: Targets for cancer therapy. Nature Reviews. Cancer. 2004;**4**:361-370

[45] Mendelsohn J, Baselga J. The EGF receptor family as targets for cancer therapy. Oncogene. 2000;**19**:6550-6565

[46] Gómez-Llobregat J, Buceta J, Reigada R. Interplay of cytoskeletal activity and lipid phase stability in dynamic protein recruitment and clustering. Scientific Reports. 2013;**3**:2608, 1–8

[47] Kusumi A, Nakada C, Ritchie K, Murase K, Suzuki K, Murakoshi H, Kasai RS, Kondo J, Fujiwara T. Paradigm shift of the plasma membrane concept from the two-dimensional continuum fluid to the partitioned fluid: High-speed single-molecule tracking of membrane molecules. Annual Review of Biophysics and Biomolecular Structure. 2005;**34**:351-378

[48] Low-Nam ST, Lidke KA, Cutler PJ, Roovers RC, van Bergen en Henegouwen PMP, Wilson BS, Lidke DS. ErbB1 dimerization is promoted by domain co-confinement and stabilized by ligand binding. Nature Structural & Molecular Biology. 2007;**174**:395-416

[49] Huang JY, Lin CY. Exploring the stochastic dynamics of correlated movement of receptor proteins in plasma membranes in vivo. The Journal of Chemical Physics. 2015;**143**:225101-225107

[50] Hess ST, Gould TJ, Gudheti MV, Maas SA, Mills KD, Zimmerberg J. Dynamic clustered distribution of hemagglutinin resolved at 40 nm in living cell membranes discriminates between raft theories. Proceedings of the National Academy of Sciences of the United States of America. 2007;**104**:17370-17375

[51] Lingwood D, Simons K. Lipid rafts as a membrane-organizing principle. Science. 2010;**327**: 46-50

[52] Orr G, Hu D, Özgxelik S, Opresko LK, Wiley HS, Colson SD. Cholesterol dictates the freedom of EGF receptors and HER2 in the plane of the membrane. Biophysical Journal. 2005;**89**:1362-1373

[53] Ringerike T, Blystad FD, Levy FO, Madshus IH, Stang E. Cholesterol is important in control of EGF receptor kinase activity but EGF receptors are not concentrated in caveolae. Journal of Cell Science. 2002;**115**:1331-1340

[54] Linda JP, Casey L. Cholesterol levels modulate EGF receptor-mediated signaling by altering receptor function and trafficking. Biochemistry. 2002;**41**:10315-10322

[55] Shlomovitz R, Maibaum L, Schick M. A unified picture of rafts: Lipid phase behavior in a multicomponent membrane. Biophysical Journal. 2014;**106**:1979-1985

[56] Shlomovitz R, Schick M. Model of a raft in both leaves of an asymmetric lipid bilayer. Biophysical Journal. 2013;**105**:1406-1413

[57] Lingwood D, Ries J, Schwille P, Simons K. Plasma membranes are poised for activation of raft phase coalescence at physiological temperature. Proceedings of the National Academy of Sciences of the United States of America. 2008;**105**:10005-10010

[58] Mueller V, Ringemann C, Honigmann A, Schwarzmann G, Medda R, Leutenegger M, Polyakova S, Belov VN, Hell SW, Eggeling C. STED Nanoscopy reveals molecular details of cholesterol- and cytoskeleton-modulated lipid interactions in living cells. Biophysical Journal. 2011;**101**:1651-1660

[59] Baumgart T, Hunt G, Farkas E, Webb W, Feigenson G. Fluorescence probe partitioning between lo/Ld phases in lipid membranes. Biochimica et Biophysica Acta. 2007;**1768**:2182-2194

[60] Manzo C, van Zanten TS, Saha S, Torreno-Pina JA, Mayor S, Garcia-Parajo MF. PSF decomposition of nanoscopy images via Bayesian analysis unravels distinct molecular organization of the cell membrane. Scientific Reports. 2014;**4**:4353–4358

[61] Veatch SL, Machta BB, Shelby SA, Chiang EN, Holowka DA, Baird BA. Correlation functions quantify super-resolution images and estimate apparent clustering due to over-counting. PLoS One. 2012;**7**:e31457

[62] van Zanten TS, Gómez J, Manzo C, Cambi C, Buceta J, Reigada R, Garcia-Parajo MF. Direct mapping of nanoscale compositional connectivity on intact cell membranes. Proceedings of National Academy of Sciences USA. 2010;**107**:15437–15442

[63] Wang F, Wang Y, Zhang X, Zhang W, Guo S, Jin F. Recent progress of cell-penetrating peptides as new carriers for intracellular cargo delivery. Journal of Controlled Release. 2014;**174**:126-136

[64] Frankel AD, Pabo CO. Cellular uptake of the TAT protein from human immunodeficiency virus. Cell. 1988;**55**:1189-1193

[65] Vives E, Brodin P, Lebleu B. A truncated HIV-1 TAT protein basic domain rapidly translocates through the plasma membrane and accumulates in the cell nucleus. The Journal of Biological Chemistry. 1997;**272**:16010-16017

[66] Tyagi M, Rusnati M, Presta M, Giacca M. Internalization of HIV-1 tat requires cell surface heparan sulfate proteoglycans. The Journal of Biological Chemistry. 2001;**276**:3254-3261

[67] Nakase I, Tadokoro A, Kawabata N, Takeuchi T, Katoh H, Hiramoto K, Negishi M, Nomizu M, Sugiura Y, Futaki S. Interaction of arginine-rich peptides with membrane-associated proteoglycans is crucial for induction of actin organization and macropinocytosis. Biochemistry. 2007;**46**:492-501

[68] Goddette DW, Frieden C. Actin polymerization. The mechanism of action of cytochalasin D. The Journal of Biological Chemistry. 1986;**261**:15974-15980

[69] Mishra A, Lai GH, Schmidt NW, Sun VZ, Rodriguez AR, Tong R, Tang L, Cheng J, Deming TJ, Kamei DT, Wong GCL. Translocation of HIV TAT peptide and analogues induced by multiplexed membrane and cytoskeletal interactions. Proceedings of the National Academy of Sciences of the United States of America. 2011;**108**:16883-16888

[70] Nadler B, Lafon Se, Coifman RR, Kevrekidis IG. Diffusion maps, spectral clustering and reaction coordinates of dynamical systems. arXiv.org. 2008. p. arXiv:math/0503445